Available online at www.sciencedirect.com
ScienceDirect
Journal of Computational Physics 224 (2007) 637–662
JOURNAL OF COMPUTATIONAL PHYSICS
www.elsevier.com/locate/jcp

High-order, low dispersive and low dissipative explicit schemes for multiple-scale and boundary problems

Julien Berland, Christophe Bogey, Olivier Marsden, Christophe Bailly *

Laboratoire de Mécanique des Fluides et d'Acoustique, UMR CNRS 5509, Ecole Centrale de Lyon, 69134 Ecully, France

Received 17 May 2005; received in revised form 9 October 2006; accepted 12 October 2006
Available online 28 November 2006

Abstract

Explicit high-order numerical schemes are proposed for the accurate computation of multiple-scale problems and for the implementation of boundary conditions. Specific high-order node-centered finite differences and selective filters removing grid-to-grid oscillations are first designed for the discretization of the buffer region between a Δx-grid domain and $2\Delta x$-grid domain. The coefficients of these matching schemes are chosen so that the maximum order of accuracy is reached. Non-centered finite differences and selective filters are then developed with the aim of accurately computing boundary conditions. They are constructed by minimizing the dispersion and the dissipation errors in the wave number space for waves down to four points per wavelength. The dispersion and dissipation properties of the matching and the boundary schemes are described in detail, and their accuracy limits are determined, to show that these schemes calculate accurately waves with at least five points per wavelength. Test problems, including linear convection, wall reflection and acoustic scattering around a cylinder, are finally solved to illustrate the accuracy of the schemes.

Keywords: Multiple-scales problem; Boundary conditions; Explicit schemes; High order; Low dispersion; Low dissipation; Matching schemes; Non-centered schemes

1. Introduction

Since the earliest stages in computational aeroacoustics (CAA), the need for highly accurate schemes has been recognized [1]. To meet the stringent accuracy requirements of CAA, low dispersive, low dissipative and large spectral bandwidth numerical methods have been designed by optimizing their dispersion and dissipation properties in the Fourier space for low wave numbers. Available optimized finite differences are for instance the explicit dispersion-relation-preserving scheme of Tam and Webb [2] or the compact schemes of Lele [3]. Bogey and Bailly [4] also recently developed explicit finite differences and selective filters accurate for waves down to four points per wavelength, allowing the direct computation of aerodynamic noise using

* Corresponding author. Fax: +33 4 72 18 91 43.
E-mail addresses: julien.berland@ec-lyon.fr (J. Berland), christophe.bogey@ec-lyon.fr (C. Bogey), olivier.marsden@ec-lyon.fr (O. Marsden), christophe.bailly@ec-lyon.fr (C. Bailly).

0021-9991/$ - see front matter
doi:10.1016/j.jcp.2006.10.017

large eddy simulation [5,6]. These examples deal only with centered schemes designed for uniform mesh grids. However, numerical tools with similar properties are required for some local specific features of the computational domain. Two examples are given below.

First, aeroacoustics problems commonly involve a wide range of length scales. Noise sources in jet flows for example are at least one order of magnitude smaller than the wavelength of the dominant radiated acoustic field. Grid stretching can then be used to take into account both acoustic and aerodynamic length scales. However, the method is a slow way to increase mesh size, and it might generate numerical errors [4]. Multiple-scale problems can be treated alternatively by using a computational domain divided into sub-domains where mesh size is uniform. Tam and Kurbatskii [7], for instance, developed seven-point cell-centered finite differences and selective filters with this aim in view. In the present work, specific node-centered schemes are designed for the discretization of the buffer region between a Δx-grid domain and a $2\Delta x$-grid domain thanks to stencils similar to those of the schemes used on uniform grids. High-order seven- and eleven-point matching finite differences and selective filters are thus, respectively, proposed for spatial discretization and for the removal of the numerical high-frequency oscillations.

Second, the implementation of free-field boundary conditions as well as wall boundary conditions commonly involves small-stencil schemes which locally lower the order of accuracy. However, to avoid extra damping and loss of accuracy, it may be recommended to use non-centered optimized schemes with high accuracy properties. Visbal and Gaitonde [8] developed implicit non-centered finite differences and Gaitonde and Visbal [9] proposed implicit non-centered selective filters which enable acoustic and aerodynamic computations for complex geometries [10,11]. Tam and Dong [12] designed explicit non-centered seven-point finite differences optimized in the Fourier space to implement wall boundary conditions, which were applied to jet screech computation for instance [13]. Using similar optimization techniques, Lockard et al. [14] and Zhuang and Chen [15] also proposed non-centered finite difference schemes. However, non-centered selective filters optimized in the same way have not been provided. The development of appropriate explicit boundary filters is of crucial importance and must be performed with attention because standard explicit non-centered filters are unstable [16]. The boundary filters must therefore be optimized in the Fourier space to form stable algorithms. With this in mind, non-centered seven- and eleven-point explicit finite differences and selective filters, with properties optimized in the wave number space, are proposed in the present work. They are designed to allow the accurate resolution of waves with at least five points per wavelength. Note that these schemes have been recently used for the direct computation of noise radiated by flows around non-Cartesian bodies [17,18].

In the present paper, the high-order seven- and eleven-point matching schemes are described in Section 2 and the low dispersive and low dissipative seven- and eleven-point non-centered boundary schemes are shown in Section 3. Test cases are resolved at the end of each Section to highlight the properties of the developed methods with respect to the standard ones. In particular, a benchmark problem involving acoustic scattering around a cylinder is considered to assess boundary schemes for a realistic configuration. Concluding remarks are finally drawn in Section 4.

2. Matching schemes

2.1. Finite differences

A finite-difference formulation appropriate for a non-uniform grid (x_i) is introduced. The local mesh size is defined as the smallest gap between x_i and its immediate neighbors x_{i-1} and x_{i+1}, i.e.

$$\Delta x_i = \min(x_{i+1} - x_i, x_i - x_{i-1}). \tag{1}$$

Actually, $2\Delta x_i$ is the smallest wavelength that the scheme is able to resolve at the node x_i. The spatial derivative of a function f at x_i can then be approximated using a $2N$-point node-centered stencil

$$\left(\frac{\partial f}{\partial x}\right)_i = \frac{1}{\Delta x_i} \sum_{j=-N}^{N} a_j f(x_{i+j}). \tag{2}$$

In the present work, coefficients a_j are determined by canceling the first terms of the Taylor series of $f(x_{i+j})$ in (2) so that the maximum order of accuracy is reached. The development of $f(x_{i+j})$ reads

$$f(x_{i+j}) = \sum_{p=0}^{2N} \frac{\beta_{ij}^p \Delta x_i^p}{p!} f^{(p)}(x_i) + \mathcal{O}(\Delta x_i^{2N+1}), \tag{3}$$

where $\beta_{ij} = (x_{i+j} - x_i)/\Delta x_i$. Thus, according to (2), it yields

$$\left(\frac{\partial f}{\partial x}\right)_i = \frac{f(x_i)}{\Delta x_i} \sum_{j=-N}^{N} a_j + \sum_{p=1}^{2N} \sum_{\substack{j=-N \\ j\neq 0}}^{N} a_j \frac{\beta_{ij}^p \Delta x_i^{p-1}}{p!} f^{(p)}(x_i) + \mathcal{O}(\Delta x_i^{2N}). \tag{4}$$

To obtain an order of accuracy of $2N$, the coefficients a_j must be solutions of the following system of equations

$$\begin{aligned} &\sum_{j=-N}^{N} a_j = 0, \\ &\sum_{\substack{j=-N \\ j\neq 0}}^{N} a_j \beta_{ij}^p = \delta_{p1}, \quad p = 1, \ldots, 2N, \end{aligned} \tag{5}$$

where δ_{p1} is the Kronecker symbol. In the present work, sixth-order seven-point and tenth-order eleven-point finite difference schemes are designed thanks to (5) for the buffer region between a uniform Δx-mesh and a uniform $2\Delta x$-mesh shown in Fig. 1. Their coefficients are given in Tables 1 and 2. The scheme names are defined in Fig. 2: the subscript denotes the size of the stencil and the exponent indicates the point where the transition occurs.

Dispersion and dissipation properties of the finite difference schemes are obtained by taking the Fourier transform of Eq. (2) in space. The effective (complex) wave number k^* of the scheme is then defined as

$$k^* \Delta x_i = -\mathrm{i} \sum_{j=-N}^{N} a_j \mathrm{e}^{\mathrm{i}\beta_{ij} k \Delta x_i}, \tag{6}$$

where k is the exact wave number. To illustrate the scheme properties, one usually considers the advective equation where an approximated derivative $\partial/\partial x$ is processed with (2)

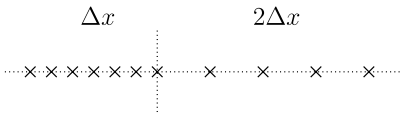

Fig. 1. Buffer region between a Δx-mesh and $2\Delta x$-mesh.

Table 1
Coefficients of the sixth-order seven-point matching finite difference schemes

	$F\mathrm{D}_7^{-2}$	$F\mathrm{D}_7^{-1}$	$F\mathrm{D}_7^{0}$	$F\mathrm{D}_7^{1}$	$F\mathrm{D}_7^{2}$
a_{-3}	−0.073881673880	−0.150000000000	−0.050793650790	−0.026041666670	−0.019047619050
a_{-2}	0.250000000000	0.812698412700	0.375000000000	0.214285714300	0.166666666700
a_{-1}	−0.833333333300	−1.500000000000	−1.371428571000	−0.937500000000	−0.800000000000
a_0	0.066666666670	0.333333333300	0.916666666700	0.300000000000	0.083333333330
a_1	0.714285714300	0.600000000000	0.150000000000	0.468750000000	0.666666666700
a_2	−0.138888888900	−0.107142857100	−0.021428571430	−0.020833333330	−0.100000000000
a_3	0.015151515150	0.011111111110	0.001984126984	0.001339285714	0.002380952381

Table 2
Coefficients of the tenth-order eleven-point matching finite difference schemes

	$F\mathrm{D}_{11}^{-4}$	$F\mathrm{D}_{11}^{-3}$	$F\mathrm{D}_{11}^{-2}$	$F\mathrm{D}_{11}^{-1}$
a_{-5}	−0.004504336385	−0.013888888830	−0.026744497310	−0.029761904800
a_{-4}	0.017857142830	0.085582391090	0.208333333200	0.272793873100
a_{-3}	−0.071428571350	−0.166666666000	−0.636519036100	−1.071428573000
a_{-2}	0.257142857000	0.333333332400	0.833333332800	2.273282276000
a_{-1}	−0.857142856900	−0.933333332000	−1.166666666000	−2.500000002000
a_0	0.022222221950	0.085714284400	0.235714285200	0.616666667500
a_1	0.818181818400	0.777777778600	0.694444444800	0.535714285200
a_2	−0.230769230800	−0.212121212500	−0.176767677000	−0.119047618800
a_3	0.057142857160	0.051282051370	0.040792540870	0.025252525190
a_4	−0.009453781515	−0.008333333343	−0.006410256426	−0.003746253734
a_5	0.000751879699	0.000653594771	0.000490196080	0.000274725274
	FD_{11}^{0}	FD_{11}^{1}	FD_{11}^{2}	FD_{11}^{3}	FD_{11}^{4}
a_{-5}	−0.005683205683	−0.002343750000	−0.001420801421	−0.001041666667	−0.000865800900
a_{-4}	0.059523809520	0.026223776220	0.016666666670	0.012626262630	0.010714290000
a_{-3}	−0.284160284200	−0.136718750000	−0.092352092350	−0.072916666670	−0.063492060000
a_{-2}	0.833333333300	0.454545454500	0.333333333300	0.277777777800	0.250000000000
a_{-1}	−1.847041847000	−1.230468750000	−1.015873016000	−0.911458333300	−0.857142900000
a_0	1.141666667000	0.496031746000	0.241666666700	0.107142857100	0.033333330000
a_1	0.119047619000	0.410156250000	0.609523809500	0.729166666700	0.800000000000
a_2	−0.019841269840	−0.019531250000	−0.095238095240	−0.166666666700	−0.214285700000
a_3	0.003607503608	0.002343750000	0.003968253968	0.026041666670	0.047619050000
a_4	−0.000485625486	−0.000253652597	−0.000288600289	−0.000694444444	−0.005952381000
a_5	0.000033300033	0.000015175796	0.000013875014	0.000022546898	0.000072150070

$$\frac{\partial u}{\partial t} + c\frac{\partial u}{\partial x} = 0. \tag{7}$$

The dispersion relation writes as follows

$$\omega = k^* c, \tag{8}$$

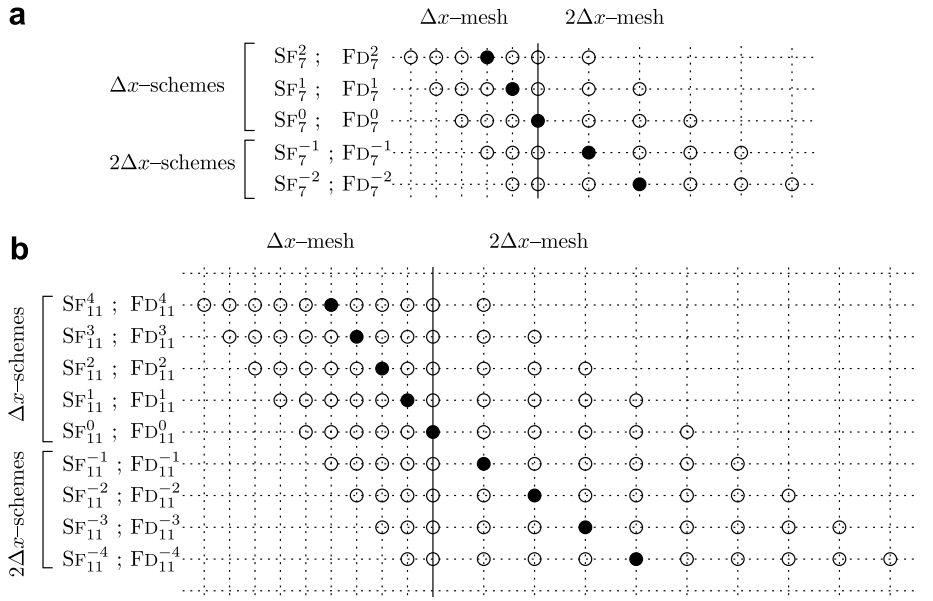

Fig. 2. Stencils and names: (a) seven-point and (b) eleven-point matching finite differences FD_N^m and selective filters SF_N^m.

where ω is the angular frequency. Take an harmonic wave $u(x,t=0)=\mathrm{e}^{\mathrm{i}kx}$ as the initial disturbance. The approximated solution of this right-running perturbation is

$$u(x,t)=\mathrm{e}^{\mathrm{i}(kx-\omega t)}. \tag{9}$$

According to (8) it can be rewritten as

$$u(x,t)=\mathrm{e}^{\mathrm{i}(kx-k^*ct)}=\underbrace{\mathrm{e}^{\mathrm{i}[k-\mathscr{R}e(k^*)]ct}}_{\text{dispersion}}\cdot\underbrace{\mathrm{e}^{\mathscr{I}m(k^*)ct}}_{\text{dissipation}}\cdot\underbrace{\mathrm{e}^{\mathrm{i}k(x-ct)}}_{\text{exact solution}}. \tag{10}$$

The phase error is given by $k\Delta x_i-\mathscr{R}e(k^*\Delta x_i)$, and the wave amplitude is multiplied by $\mathrm{e}^{\mathscr{I}m(k^*\Delta x_i)}$ for a right-running wave, and by $\mathrm{e}^{-\mathscr{I}m(k^*\Delta x_i)}$ for a left-running wave, propagating over a distance Δx_i. For brevity, in what follows, only the eleven-point schemes are described in detail, but a similar analysis could be made for the seven-point schemes.

The phase error defined by expression (10) corresponds to the error introduced by the semi-discrete approximation of Eq. (7) for a plane harmonic wave. For non-harmonic waves however, the crests of the waves still propagate at the phase speed $v_\varphi=\omega/k=ck^*/k$, but the energy of the wave-packet moves at the group velocity [19], $v_\mathrm{g}=\partial\omega/\partial k=c\partial k^*/\partial k$. This point is particularly well illustrated numerically in [20] for instance. The phase and group velocities are directly related in finite-difference schemes. The phase error is thus used in the present study as a good indicator for measuring the behavior of the schemes, but does not correspond to the exact numerical error for non-harmonic problems, for which the group velocity is more relevant.

The dispersion error $|k\Delta x_i-\mathscr{R}e(k^*\Delta x_i)|/\pi$ is plotted for the eleven-point schemes in Fig. 3a for the Δx-schemes ($\Delta x_i=\Delta x$) and in Fig. 4a for the $2\Delta x$-schemes ($\Delta x_i=2\Delta x$) as a function of $k\Delta x$, in logarithmic scales. The centered tenth-order eleven-point scheme obtained on a uniform grid is also plotted for comparison. It is referred to as $\mathrm{FD}_{11}^{\mathrm{unif}}$. The cut-off wave number of the $2\Delta x$-schemes is $k_c\Delta x=\pi/2$. Indeed, grid-to-grid oscillations corresponding to two points per wavelength waves on a $2\Delta x$-mesh correspond to four points per wavelength waves on a Δx mesh spacing. The dispersion errors remain lower than 5×10^{-3} up to about $k\Delta x<\pi/2$ for all the Δx-schemes and up to $k\Delta x<\pi/4$ for all the $2\Delta x$-schemes. These limits in wave number correspond, respectively, to four and eight points per wavelength with respect to the Δx mesh spacing. Grid-to-grid waves, $k\Delta x=\pi$ on the Δx-mesh and $k\Delta x=\pi/2$ on the $2\Delta x$-mesh, are moreover not resolved.

The amplification factor $\mathrm{e}^{\pm\mathscr{I}m(k^*\Delta x_i)}$ for the eleven-point schemes is now plotted in Fig. 3b for the Δx-schemes and in Fig. 4b for the $2\Delta x$-schemes as a function of $k\Delta x$, in logarithmic scales. For low wave numbers, i.e. about $k\Delta x<\pi/2$ for the Δx-schemes and $k\Delta x<\pi/4$ for the $2\Delta x$-schemes, the amplification factors remain close to 1. For higher wave numbers, and especially for grid-to-grid oscillations, the amplification factor is such that $\mathrm{e}^{\mathscr{I}m(k^*\Delta x_i)}<1$ and $\mathrm{e}^{-\mathscr{I}m(k^*\Delta x_i)}>1$. Left-running waves are therefore amplified and right-running waves are dissipated. These non-resolved waves will have to be removed by using selective filters.

For quantitative comparisons, limits of accuracy in phase and amplitude are determined respectively through the criteria $|k\Delta x_i-\mathscr{R}e(k^*\Delta x_i)|/\pi<5\times10^{-3}$ and $|1-\mathrm{e}^{\mathscr{I}m(k^*\Delta x_i)}|<5\times10^{-3}$. These limits are reported

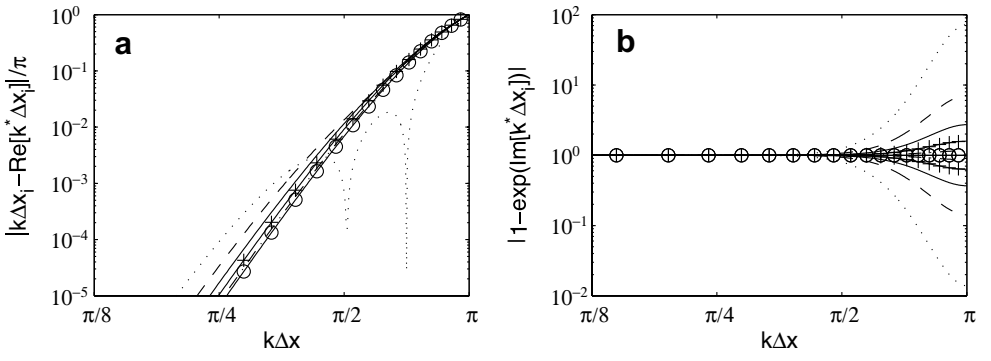

Fig. 3. (a) Dispersion, and (b) dissipation errors of the eleven-point matching Δx-schemes as functions of the wave number $k\Delta x$: —o— $\mathrm{FD}_{11}^{\mathrm{unif}}$, –·–·–·– FD_{11}^{4}, —+— FD_{11}^{3}, — FD_{11}^{2}, – – – FD_{11}^{1}, ··· FD_{11}^{0}.

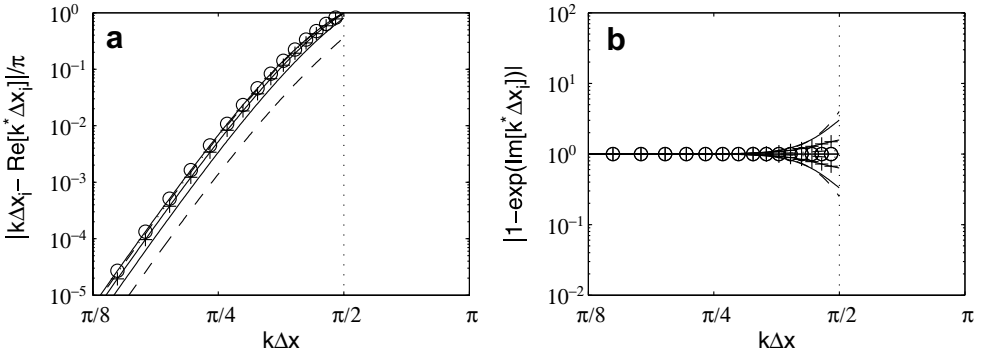

Fig. 4. (a) Dispersion, and (b) dissipation errors of the eleven-point matching $2\Delta x$-schemes as functions of the wave number $k\Delta x$: ——o—— $\mathrm{FD}_{11}^{\mathrm{unif}}$, ——+—— FD_{11}^{-1}, – – – FD_{11}^{-2}, — FD_{11}^{-3}, –·–·– FD_{11}^{-4}. The dotted line shows the cut-off wave number of the schemes with respect to the Δx mesh spacing.

in Table 3 in terms of points per wavelength, given with respect to the Δx mesh spacing for all schemes. The limits of accuracy of the centered tenth-order eleven-point finite differences $\mathrm{FD}_{11}^{\mathrm{unif}}$ for uniform grids are also given both on the Δx and the $2\Delta x$ grids. This scheme does not introduce any dissipation since it is symmetric. Due to dispersion errors, it is however accurate for waves down to four points per wavelength, that is $\lambda = 4\Delta x$ on the Δx-grid or $\lambda = 8\Delta x$ on the $2\Delta x$-grid. The limits of accuracy of the matching schemes, both in phase and in amplitude, are very similar, about $\lambda = 4\Delta x$ for the Δx-schemes and $\lambda = 8\Delta x$ on the $2\Delta x$-schemes.

These limits of accuracy show that the present eleven-point matching finite differences permit waves discretized by eight points per wavelength on the Δx-mesh, or equivalently discretized by four points on the $2\Delta x$-mesh, to travel through the buffer region properly. Smaller wavelengths are not accurately resolved and have therefore to be removed by selective filtering.

2.2. Selective filters

To remove grid-to-grid oscillations, the selective filtering of a function f can be performed as follows:

$$f^d(x_i) = f(x_i) - \sigma \sum_{j=-N}^{N} d_j f(x_{i+j}), \tag{11}$$

Table 3
Dispersion and dissipation limits of the eleven-point matching finite differences in points per wavelength $\lambda/\Delta\, x = 2\pi/k\Delta x$ with respect to the Δx mesh spacing

	Dispersion $\lvert k\Delta x_i - \mathscr{R}e(k^*\Delta x_i)\rvert/\pi < 5\times 10^{-3}$	Dissipation $\lvert 1 - \mathrm{e}^{\mathscr{I}m(k^*\Delta x_i)}\rvert < 5\times 10^{-3}$
	$\lambda/\Delta x$	$\lambda/\Delta x$
$\mathrm{FD}_{11/\Delta x}^{\mathrm{unif}}$	4.14	0
FD_{11}^{4}	4.19	3.67
FD_{11}^{3}	4.28	4.24
FD_{11}^{2}	4.41	4.75
FD_{11}^{1}	4.56	5.35
FD_{11}^{0}	3.66	6.23
FD_{11}^{-1}	6.96	7.63
FD_{11}^{-2}	7.68	7.81
FD_{11}^{-3}	8.04	7.54
FD_{11}^{-4}	8.21	6.79
$\mathrm{FD}_{11/2\Delta x}^{\mathrm{unif}}$	8.28	0

The limits of the standard centered tenth-order scheme are also given when the scheme is used on a uniform Δx-grid ($\mathrm{FD}_{11/\Delta x}^{\mathrm{unif}}$) and on a uniform $2\Delta x$-grid ($F\mathrm{D}_{11/2\Delta x}^{\mathrm{unif}}$).

where f^d is the filtered function, and d_j are the stencil coefficients. The parameter σ is a constant, taken between 0 and 1, defining the filtering strength. In practice, in numerical simulations, since filtering is applied to the flow variables every iteration, or every second iteration for instance [6], it is not necessary to set σ to 1, and smaller values are used. Nevertheless, in order to design the filter in the present work, the filtering strength is set to its maximum value $\sigma = 1$. Consider the spatial Fourier transform of (11) to compute the transfer function of the filter

$$G(k\Delta x_i) = 1 - \sum_{j=-N}^{N} d_j \mathrm{e}^{\mathrm{i}\beta_{ij}k\Delta x_i} \tag{12}$$

with the Δx_i and β_{ij} defined in Section 2.1. To determine the coefficients d_j, the first terms resulting from the Taylor series of (12) obtained as $k\Delta x_i \to 0$

$$G(k\Delta x_i) = 1 - \sum_{j=-N}^{N} d_j - \sum_{p=1}^{2N-1} \frac{(\mathrm{i}k\Delta x_i)^p}{p!} \left[\sum_{j=-N}^{N} \beta_{ij}^p d_j \right] + \mathrm{O}(k\Delta x_i^{2N}) \tag{13}$$

are canceled, where $\beta_{ij} = (x_{i+j} - x_i)/\Delta x_i$. Enforcing the two following criteria

$$\begin{aligned} &G(k) = 1 + \mathcal{O}(k\Delta x_i^{\gamma}), \quad \text{as } k \to 0, \\ &G(\pi) = 0, \end{aligned} \tag{14}$$

then yields a system of equations to determine the d_j coefficients ensuring an accuracy of order γ, as $k \to 0$.

For the Δx-schemes, the β_{ij} coefficients are integers and Eqs. (13) and (14) are rewritten as

$$\begin{aligned} &\sum_{j=-N}^{N} (-1)^{\beta_{ij}} d_j = 1, \\ &\sum_{j=-N}^{N} d_j = 0, \\ &\sum_{j=-N}^{N} d_j \beta_{ij}^p = 0, \quad p = 1, \ldots, 2N-1 \end{aligned} \tag{15}$$

with $\gamma = 2N$. Seven-point sixth-order and eleven-point tenth-order Δx-selective filters are built up using this system of equations.

Consider now the $2\Delta x$-schemes. Coefficients β_{ij} are no longer integers and the condition $G(\pi) = 0$ is a priori complex and yields two scalar equations on the coefficients d_j:

$$\begin{aligned} &\sum_{j=-N}^{N} \cos(\beta_{ij}\pi) d_j = 1, \\ &\sum_{j=-N}^{N} \sin(\beta_{ij}\pi) d_j = 0, \\ &\sum_{j=-N}^{N} d_j = 0, \\ &\sum_{j=-N}^{N} d_j \beta_{ij}^p = 0, \quad p = 1, \ldots, 2N-2. \end{aligned} \tag{16}$$

The order of accuracy is then reduced down to $\gamma = 2N - 1$. Seven-point fifth-order and eleven-point ninth-order $2\Delta x$-selective filters are designed here in this way.

The scheme coefficients are given in Tables 4 and 5. The stencil names are defined as in Fig. 2. Remark that the coefficient d_5 of the Δx-filter SF_{11}^0 is optimized so that the filter remains stable with $|G(k\Delta x_i)| < 1$ for $k\Delta x_i \in [0, \pi]$. In this case, the order of accuracy of the scheme has to be reduced down to nine.

Table 4
Coefficients of the seven-point matching selective filters

	SF_7^{-2}	SF_7^{-1}	SF_7^{0}	SF_7^{1}	SF_7^{2}
d_{-3}	0.000000000000	0.031250000000	−0.050000000000	−0.027343750000	−0.018750000000
d_{-2}	0.031250000000	0.000000000000	0.246093750000	0.150000000000	0.109375000000
d_{-1}	−0.156250000000	−0.156250000000	−0.450000000000	−0.328125000000	−0.262500000000
d_0	0.312500000000	0.312500000000	0.328125000000	0.350000000000	0.328125000000
d_1	−0.312500000000	−0.312500000000	−0.098437500000	−0.164062500000	−0.218750000000
d_2	0.156250000000	0.156250000000	0.028125000000	0.021875000000	0.065625000000
d_3	−0.031250000000	−0.031250000000	−0.003906250000	−0.002343750000	−0.003125000000

Table 5
Coefficients of the eleven-point matching selective filters

	SF_{11}^{-4}	SF_{11}^{-3}	SF_{11}^{-2}	SF_{11}^{-1}
d_{-5}	0.000000000000	0.001953125000	0.009945609941	0.027343749990
d_{-4}	0.001953125000	0.000000000000	−0.035156249990	−0.149184149100
d_{-3}	−0.017578125000	−0.017578125000	0.009945609941	0.281249999900
d_{-2}	0.070312500000	0.070312500000	0.072916666650	−0.149184149100
d_{-1}	−0.164062500000	−0.164062500000	−0.167708333300	−0.109375000000
d_0	0.246093750000	0.246093750000	0.243750000000	0.218750000000
d_1	−0.246093750000	−0.246093750000	−0.238715277800	−0.210937500000
d_2	0.164062500000	0.164062500000	0.156881313200	0.135416666700
d_3	−0.070312500000	−0.070312500000	−0.066542832180	−0.056344696980
d_4	0.017578125000	0.017578125000	0.016506410260	0.013767482520
d_5	−0.001953125000	−0.001953125000	−0.001822916667	−0.001502403847

	SF_{11}^{0}	SF_{11}^{1}	SF_{11}^{2}	SF_{11}^{3}	SF_{11}^{4}
d_{-5}	0.006225476190	−0.002909342448	−0.001860119048	−0.001342773438	−0.001085069444
d_{-4}	−0.023421835937	0.026041666670	0.017456054690	0.013020833330	0.010742187500
d_{-3}	−0.019044285714	−0.101826985700	−0.072544642860	−0.056396484380	−0.047743055560
d_{-2}	0.238418984375	0.225694444400	0.174560546900	0.143229166700	0.125325520800
d_{-1}	−0.487181190476	−0.305480957000	−0.265997023800	−0.234985351600	−0.214843750000
d_0	0.384474492188	0.248263888900	0.261840820300	0.257812500000	0.250651041700
d_1	−0.149023236607	−0.101826985700	−0.159598214300	−0.187988281200	−0.200520833300
d_2	0.068834975818	0.014546712240	0.049874441960	0.085937500000	0.107421875000
d_3	−0.023998783482	−0.002909342448	−0.004156203497	−0.020141601560	−0.035807291670
d_4	0.005245403646	0.000440809462	0.000453404018	0.000895182292	0.005967881944
d_5	−0.000530000000	−0.000033908420	−0.000029064360	−0.000040690104	−0.000108506944

To investigate the filter properties in the Fourier space, the frequency response function is recasted into the following form:

$$G(k\Delta x) = |G|\mathrm{e}^{\mathrm{i}\phi_G} \tag{17}$$

where $|G|$ is the modulus and ϕ_G denotes the argument of G. For brevity, we focus on the features of the eleven-point schemes. The amount of dissipation $1 - |G(k\Delta x_i)|$ and the phase error $|\phi_G(k\Delta x_i)|/\pi$ are plotted for the eleven-point filters in Fig. 5a for the Δx-filters and in Fig. 6a for the $2\Delta x$-filters as functions of $k\Delta x$, in logarithmic scales. They are compared to the tenth-order eleven-point standard centered selective filter used on uniform grids, referred to as $\mathrm{SF}_{11}^{\mathrm{unif}}$. The dissipation of the Δx- and $2\Delta x$-filters is close to the dissipation of the centered filter. As expected, dissipation is significant for grid-to-grid oscillations, but it is negligible for low wave numbers thanks to the high order. It is lower than 5×10^{-3} up to $k\Delta x < \pi/2.5$ for the Δx-filters and up to $k\Delta x < \pi/5$ for the $2\Delta x$-filters. These wave number limits correspond, respectively, to $\lambda = 5\Delta x$ on the Δx-mesh and $\lambda = 10\Delta x$ on the $2\Delta x$-mesh.

The phase errors are presented in Figs. 5b and 6b. They are lower than 5×10^{-3} up to about $k\Delta x < \pi/2.5$ for the Δx-filters and up to $k\Delta x < \pi/5$ for the $2\Delta x$-filters. For high wave numbers, $k\Delta x \simeq \pi$ for the Δx-filters and

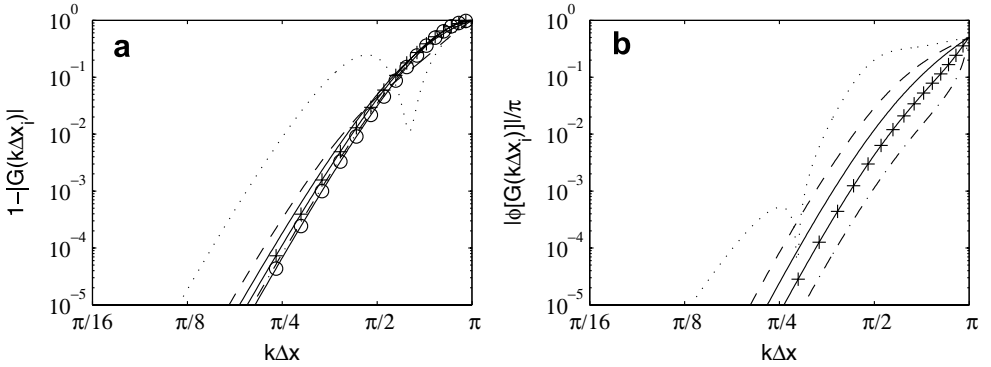

Fig. 5. (a) Amount of dissipation, and (b) phase error of the eleven-point matching Δx-selective filters as functions of the wave number $k\Delta x$: —o— $\mathrm{SF}_{11}^{\mathrm{unif}}$, —+— SF_{11}^{4}, – – – SF_{11}^{3}, — SF_{11}^{2}, – – – SF_{11}^{1}, $\cdots$ SF_{11}^{0}.

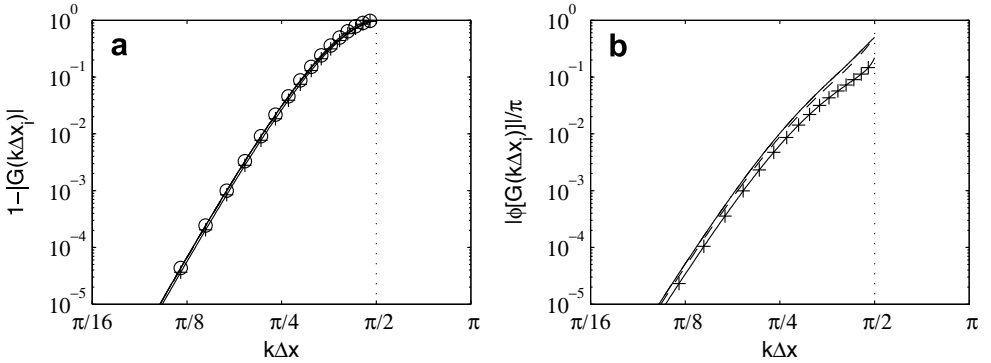

Fig. 6. (a) Amount of dissipation, and (b) phase error of the eleven-point matching $2\Delta x$-selective filters as functions of the wave number $k\Delta x$: —o— $\mathrm{SF}_{11}^{\mathrm{unif}}$, —+— SF_{11}^{-1}, – – – SF_{11}^{-2}, — SF_{11}^{-3}, –·–·– SF_{11}^{-4}. The dotted line shows the cut-off wave number of the schemes with respect to the Δx mesh spacing.

$k\Delta x \simeq \pi/2$ for the $2\Delta x$-filters, the phase errors become significant but these waves are precisely those which are filtered out.

To compare the filter properties quantitatively, limits in dissipation and dispersion are estimated from the criteria, $1 - |G(k\Delta x_i)| < 5 \times 10^{-3}$ and $|\phi_G(k\Delta x_i)|/\pi < 5 \times 10^{-3}$, based on half a percent error as in Section 2.1. The results are reported in Table 6 in terms of wavelengths with respect to the Δx mesh spacing. The dissipation limit of the centered filter $\mathrm{SF}_{11}^{\mathrm{unif}}$ is also provided, about $\lambda = 5\Delta x$ on the Δx-mesh and $\lambda = 10\Delta x$ on the $2\Delta x$-mesh. The limits of accuracy of the matching filters appear to be very close to these values. The dissipation and dispersion limits of these schemes are indeed about $\lambda = 5\Delta x$ for the Δx-filters and $\lambda = 10\Delta x$ for the $2\Delta x$-filters.

The present eleven-point matching filters are thus shown to remove only waves with wavelengths smaller than $\lambda = 10\Delta x$. As a result, waves discretized by at least five points on the $2\Delta x$-mesh or equivalently by at least 10 points on the Δx-mesh are not affected significantly when they propagate through the buffer region.

2.3. Test problems

2.3.1. Linear convection

The properties of the matching schemes are illustrated by solving the advection equation

$$\frac{\partial u}{\partial t} + \epsilon c \frac{\partial u}{\partial x} = 0, \tag{18}$$

Table 6
Dissipation and phase error limits of the eleven-point matching selective filters in points per wavelength $\lambda/\Delta x = 2\pi/k\Delta x$ with respect to the Δx mesh spacing

	Dissipation $1 - \lvert G(k\Delta x_i)\rvert < 5\times 10^{-3}$	Phase error $\lvert\phi_G(k\Delta x_i)\rvert/\pi < 5\times 10^{-3}$
	$\lambda/\Delta x$	$\lambda/\Delta x$
$\mathrm{SF}^{\mathrm{unif}}_{11/\Delta x}$	4.99	0
SF^{4}_{11}	5.07	3.30
SF^{3}_{11}	5.22	3.92
SF^{2}_{11}	5.44	4.48
SF^{1}_{11}	5.68	5.08
SF^{0}_{11}	8.58	6.06
SF^{-1}_{11}	9.79	8.30
SF^{-2}_{11}	9.94	8.73
SF^{-3}_{11}	9.97	8.89
SF^{-4}_{11}	9.97	8.89
$\mathrm{SF}^{\mathrm{unif}}_{11/2\Delta x}$	9.98	0

The limits of the standard centered tenth-order filter are also given when the filter is used on a uniform Δx-grid ($\mathrm{SF}^{\mathrm{unif}}_{11/\Delta x}$) and on a uniform $2\Delta x$-grid ($\mathrm{SF}^{\mathrm{unif}}_{11/2\Delta x}$).

where $\epsilon = 1$ for right-running waves and $\epsilon = -1$ for left-running waves, and $c = 1$. The grid is non-uniform: at $x = 0$ the mesh size changes from Δx to $2\Delta x$ as shown in Fig. 7a, with $\Delta x = 1$. Initial disturbances at $t = 0$ are defined as

$$u_0(x) = \cos\left[\frac{2\pi}{a\Delta x}(x - x_0)\right]\exp\left[-\ln(2)\left(\frac{x - x_0}{b\Delta x}\right)^2\right], \tag{19}$$

where $a\Delta x$ is the dominant wavelength, $b\Delta x$ is the half-width of the Gaussian function and x_0 is the initial axial location of the perturbation. Right- and left-running waves with the same spectral content are propagated here. The parameters of the two cases are:

1. right-running wave: $\epsilon = 1$, $a = 10$, $b = 12$, $x_0 = -30$;
2. left-running wave: $\epsilon = -1$, $a = 10$, $b = 12$, $x_0 = 30$.

The dominant wavelength $a\Delta x = 10\Delta x$ corresponds to a signal with 10 points per wavelength with respect to the Δx mesh spacing and to a five points per wavelength wave with respect to the $2\Delta x$ mesh spacing. The

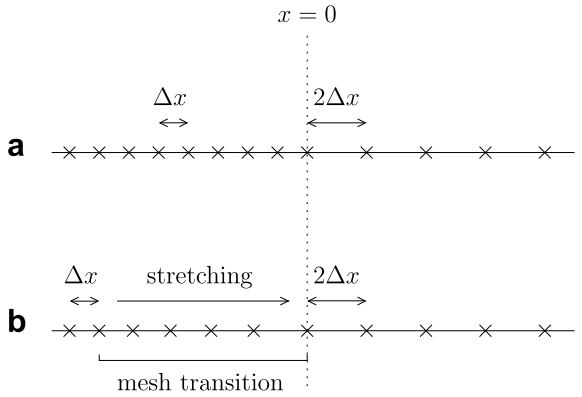

Fig. 7. Mesh size change for the linear convection problems: (a) the domain is divided into two uniform grids of mesh size Δx and $2\Delta x$, and (b) the Δx-mesh is stretched so that mesh size is equal to $2\Delta x$ at $x = 0$.

Gaussian half-width is chosen so that the spectral content of the initial perturbation does not contain waves discretized by less than four points per wavelength in the $2\Delta x$-mesh. The solution is computed up to $t = 60$. The optimized six-stage Runge–Kutta algorithm developed by Bogey and Bailly [4] is used for time integration with a CFL $= c\Delta t/\Delta x$ number equal to 0.8. Two filtering strengths are tested: $\sigma = 0.2$ and $\sigma = 0.8$. Optimized eleven-point finite-differences and selective filtering [4] are implemented to discretize the wave equation in the regions where the grid is uniform. These centered schemes calculate accurately waves with at least four points per wavelength. The matching eleven-point finite-differences and selective filters are finally applied to the buffer regions between the uniform-mesh sub-domains.

The initial perturbations and the solutions computed at $t = 60$, for $\sigma = 0.2$, are plotted in Figs. 8 and 9 for the right- and the left-running waves, respectively. No notable dissipation nor dispersion appears to be generated when the wave crosses the buffer region. Indeed, after the buffer region, the computed wave shape fits the exact solution very well in both right- and left-running cases. The solutions obtained at $t = 60$ for $\sigma = 0.8$ are given in Fig. 10a for the right-running wave, and in Fig. 10b for the left-running wave. In both cases, the computed wave is slightly dissipated, but it still remains in good agreement with the exact solution.

The problem is now solved using the same numerical procedure and the same mesh as above, but with the following parameters for the initial perturbation: $\epsilon = 1$, $a = 5$, $b = 12$, $x_0 = -30$. The filtering strength σ is set to 0.2. The initial perturbation, which is plotted in Fig. 11a, is a right-running wave discretized by five points per wavelength on the Δx-mesh. It is thus well resolved by the numerical methods on the Δx-grid. However, the wave contains only 2.5 points per wavelength on the $2\Delta x$-mesh. As a result, it cannot be propagated accurately in the coarse mesh and should be removed when it moves into the coarse grid region. The solution

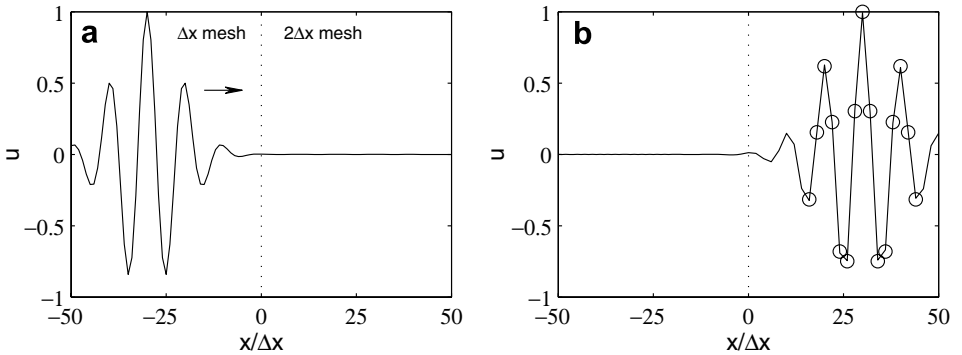

Fig. 8. (a) Initial perturbation, and (b) computed solution at $t = 60$ for the right-running wave for $\sigma = 0.2$ (○ exact solution). The arrow shows the direction of propagation.

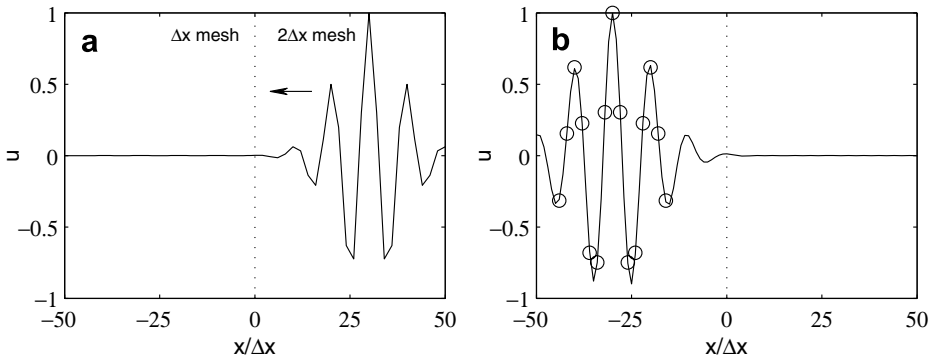

Fig. 9. (a) Initial perturbation, and (b) computed solution at $t = 60$ for the left-running wave for $\sigma = 0.2$ (○ exact solution). The arrow shows the direction of propagation.

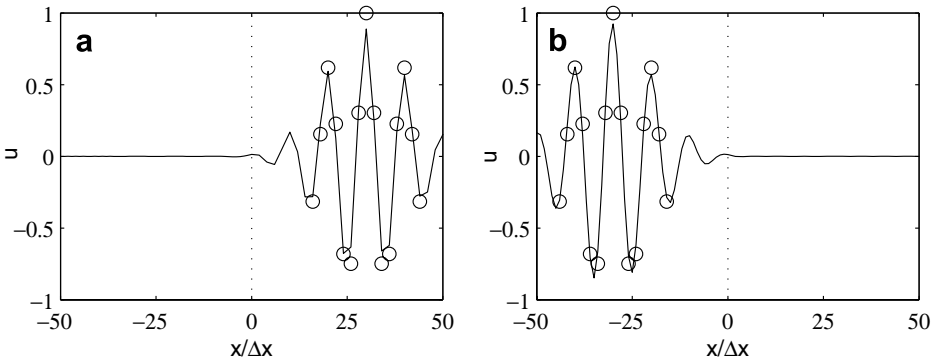

Fig. 10. Computed solutions at $t = 60$ with a filtering strength σ equal to 0.8, (a) for the right-running wave, and (b) for the left-running wave (○ exact solution).

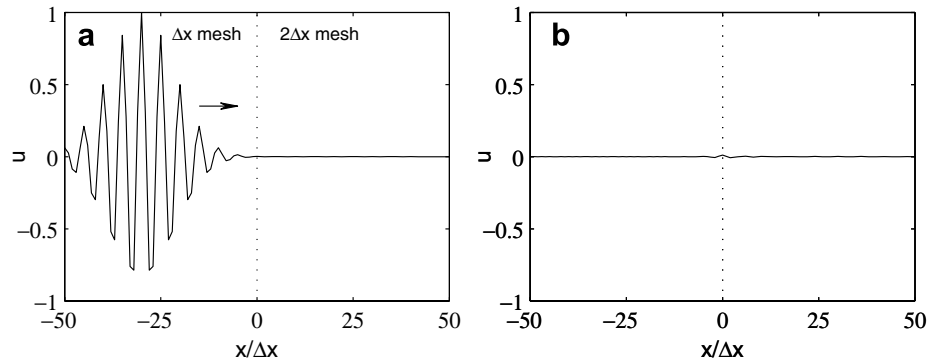

Fig. 11. (a) Initial perturbation, and (b) computed solution at $t = 60$ for a right-running wave which is not resolved in the $2\Delta x$-mesh, with $\sigma = 0.2$. The arrow shows the direction of propagation.

computed at $t = 60$ is shown in Fig. 11b. At $t = 60$, the wave, that should theoretically be observed at $x/\Delta x \simeq 30$ is found to be completely damped. It is also important to note that no spurious oscillations appears to be produced at the mesh transition.

2.3.2. Comparison to grid stretching

A test case is now solved using either the matching schemes or grid stretching for the buffer region, in order to compare the accuracy of the two methods. The convective wave Eq. (18) is solved with the initial perturbation (19). The initial perturbation is a right-running wave, *i.e.* $\epsilon = 1$, placed at $x_0 = -100\Delta x$. In a first calculation, a uniform Δx-mesh and a uniform $2\Delta x$-mesh are connected at $x = 0$ as shown in Fig. 7a. In this case, the matching schemes developed in the present work are used in the buffer region, and the standard tenth-order schemes are implemented in the regions of uniform grid. Two other calculations are performed using grid stretching so that the mesh size equals exactly $2\Delta x$ at $x = 0$, as illustrated in Fig. 7b. The two stretching rates $r = 1.014$ and $r = 1.071$ are used. The mesh transition is then built up over 50 points and 10 points, respectively. The standard tenth-order finite-differences and selective filters are implemented in the regions of uniform grid as well as in the region of stretched grid. In order to implement these schemes on the stretched grids, a mapping to a uniform mesh is built up. Following Fletcher [21], the mesh metrics and the derivatives of the variables are then computed with the same scheme. In all cases, the optimized six-stage Runge–Kutta algorithm developed by Bogey and Bailly [4] is used for time integration with a CFL $= c\Delta t/\Delta x$ number equal to 0.8, and the filtering strength is $\sigma = 0.2$.

Table 7
Linear convection test case

	Matching schemes	1.4% Stretching	7.1% Stretching
$\lambda = 10\Delta x$	5.7×10^{-3}	6.8×10^{-3}	6.3×10^{-3}
$\lambda = 12\Delta x$	1.3×10^{-3}	2.0×10^{-3}	1.9×10^{-3}
$\lambda = 16\Delta x$	1.3×10^{-4}	2.8×10^{-4}	2.6×10^{-4}

L_2 errors obtained at $t = 200$ for various dominant wavelengths of the initial perturbations with respect to the Δx mesh spacing, for the different mesh configurations.

The test case is solved with $b = 12$, and a is successively set to 10, 12 and 16 so that the dominant wavelength of the initial perturbation (19) corresponds to signals with five, six and eight points per wavelength on the $2\Delta x$-mesh. The solution is computed up to $t = 200$ and the error is given by the L_2-norm defined as

$$L_2 = \sqrt{\frac{\sum_{x>0}(u - u_e)^2}{\sum_{x>0} u_e^2}}, \tag{20}$$

where u and u_e are, respectively, the computed and the exact vector solution. Note that the L_2-norm is computed using only the mesh points that are common to all the mesh configurations, i.e. those with a positive abscissa.

The error is given in Table 7 at $t = 200$ for the different test cases. As expected, the error increases as the number of points per wavelength decreases. The accuracy is especially shown to be higher using the matching schemes for the three initial perturbations. For the perturbation with a dominant wavelength $\lambda = 16\Delta x$, the error using the matching schemes is for instance half that obtained for the two configurations with mesh stretching. For $\lambda = 12\Delta x$ and $\lambda = 10\Delta x$, the gain in accuracy due to the matching schemes is lower, but remains around 30% for $\lambda = 12\Delta x$ and 10% for $\lambda = 10\Delta x$. For the three initial perturbations, the numerical errors of the stretched configurations are similar for the stretching rates $r = 1.014$ and $r = 1.071$. A higher stretching rate implies larger numerical errors but these errors are introduced at a smaller number of mesh points. These opposite trends may explain why the error remains fairly constant as the stretching rate varies.

3. Boundary schemes

3.1. Finite differences

On a uniform grid (x_i), the spatial derivative of a function f can be approximated using a non-centered finite difference scheme by

$$\left(\frac{\partial f}{\partial x}\right)_i = \frac{1}{\Delta x} \sum_{j=-P}^{Q} a_j f(x_i + j\Delta x), \tag{21}$$

where Δx is the mesh spacing and a_j are the stencil coefficients. The approximation uses P points left to x_i and Q points right to x_i. Applying Fourier transform in space to (21) yields the effective wave number k^* of the scheme

$$k^* \Delta x = -\mathrm{i} \sum_{j=-P}^{Q} a_j \mathrm{e}^{\mathrm{i}jk\Delta x}. \tag{22}$$

In the present work, following Tam and Webb [2] for instance, coefficients a_j are determined to minimize the phase error and the dissipation provided by the scheme, as discussed in Section 2.1. Note again that the numerical error is imposed by the group velocity for non-harmonic problems. However, the phase and group velocities are intimately related, and the present optimization performed on the effective wavenumber leads to small errors on these two velocities.

First, to ensure a minimum order of accuracy, the terms of the Taylor series of (21) are canceled up to the fourth order. Coefficients a_j are then determined to minimize the integral error defined by

Table 8
Parameters α used in the development of the non-centered finite differences and selective filters

Seven-point finite differences	FD_{06}	FD_{15}	FD_{24}		
α	0.25	0.5	0.5		
Eleven-point finite differences	FD_{010}	FD_{19}	FD_{28}	FD_{37}	FD_{46}
α	0.9	0.9	0.5	0.5	0.5
Seven-point selective filters	SF_{15}	SF_{24}			
α	0.9	1			
Eleven-point selective filters	SF_{28}	SF_{37}	SF_{46}		
α	1	1	1		

$$\int_{\pi/16}^{\pi/2} [(1-\alpha)|k\Delta x - \mathscr{R}e(k^*\Delta x)| + \alpha|\mathscr{I}m(k^*\Delta x)|] \frac{\mathrm{d}(k\Delta x)}{k\Delta x}, \tag{23}$$

where the parameter α is chosen between 0 and 1 depending on the scheme. The aim is to provide homogeneous properties for the designed schemes, by balancing the errors due to dispersion and dissipation during the optimization. Several values of α have been tested. A change in the value of α of the order of 0.1 was noticed for instance to make the optimization algorithm converge toward a different solution. The values of α used for the proposed schemes are given in Table 8. The bounds of the integral are arbitrarily chosen to optimize the wave numbers between $k\Delta x = \pi/16$ (32 by points per wavelength) and $k\Delta x = \pi/2$ (4-point per wavelength). Fourth-order seven- and eleven-point non-centered finite-difference schemes FD_{PQ} have been designed in this way. Their coefficients are given in Tables 9 and 10 and a sketch of the stencils for these schemes is shown in Fig. 12.

The dispersion and dissipation properties of the seven-point finite differences are plotted in Figs. 13a and b, respectively, as functions of $k\Delta x$, in logarithmic scales. In the same way, those of the eleven-point finite differences are shown in Figs. 13c and 13d, where the features of the eleven-point centered optimized finite differences FD_{55} built by Bogey and Bailly [4] are reported for comparison. The dispersion errors $|k\Delta x - \mathscr{R}e(k^*\Delta x)|/\pi$ of the non-centered schemes are lower than 5×10^{-3} up to about $k\Delta x = \pi/2.5$, corresponding to five points per wavelength. In particular, the dispersion of the eleven-point non-centered schemes appears fairly similar to that of the centered scheme in Fig. 13c. In Figs. 13b and d, the amplification factors $\mathrm{e}^{\pm\mathscr{I}m(k^*\Delta x)}$ of the non-centered schemes are nearly equal to 1 for wave numbers lower than $k\Delta x = \pi/2.5$. The amplitude of the corresponding waves are thus not significantly modified by these differentiation schemes. On the contrary, grid-to-grid oscillations with $k\Delta x \sim \pi$ are either damped or amplified. Indeed, close to $k\Delta x = \pi$, we observe that $\mathrm{e}^{\mathscr{I}m(k^*\Delta x)} < 1$ and $\mathrm{e}^{-\mathscr{I}m(k^*\Delta x)} > 1$, implying that left-running waves are amplified and right-running waves are damped.

Criteria of accuracy based on half a percent error, $|k\Delta x - \mathscr{R}e(k^*\Delta x)|/\pi < 5\times10^{-3}$ and $|1-\mathrm{e}^{\mathscr{I}m(k^*\Delta x)}| < 5\times10^{-3}$, are introduced to illustrate, respectively, the dispersion and the dissipation errors. The accuracy limits are given in Table 11 for the different eleven-point boundary schemes. Those of the centered optimized finite differences are also provided for comparison. The non-centered schemes FD_{46} and FD_{37} have dispersion limits close to four points per wavelength, which are similar to the limit of accuracy of the centered scheme.

Table 9
Coefficients of the seven-point non-centered finite differences

	FD_{24}	FD_{15}	FD_{06}
a_{-2}	0.048264094108		
a_{-1}	−0.488255830845	−0.212932721951	
a_0	−0.366015590723	−1.060320390770	−2.225833963270
a_1	1.048005455857	2.078926116439	4.827779580575
a_2	−0.289325926394	−1.287179452384	−5.001388453836
a_3	0.050392437692	0.685176395471	3.911103941646
a_4	−0.003064639693	−0.245320613994	−2.115267458633
a_5		0.041650667189	0.718882784412
a_6			−0.115276430895

Table 10
Coefficients of the eleven-point non-centered finite differences

i	F_{D46}	F_{D37}	F_{D28}	F_{D19}	F_{D010}
a_{-4}	0.016756572303				
a_{-3}	−0.117478455239	−0.013277273810			
a_{-2}	0.411034935097	0.115976072920	0.057982271137		
a_{-1}	−1.130286765151	−0.617479187931	−0.536135360383	−0.180022054228	
a_0	0.341435872100	−0.274113948206	−0.264089548967	−1.237550583044	−2.391602219538
a_1	0.556396830543	1.086208764655	0.917445877606	2.484731692990	5.832490322294
a_2	−0.082525734207	−0.402951626982	−0.169688364841	−1.810320814061	−7.650218001182
a_3	0.003565834658	0.131066986242	−0.029716326170	1.112990048440	7.907810563576
a_4	0.001173034777	−0.028154858354	0.029681617641	−0.481086916514	−5.922599052629
a_5	−0.000071772671	0.002596328316	−0.005222483773	0.126598690230	3.071037015445
a_6	−0.000000352273	0.000128743150	−0.000118806260	−0.015510730165	−1.014956769726
a_7		0.0	−0.000118806260	0.000021609059	0.170022256519
a_8			−0.000020069730	0.000156447571	0.002819958377
a_9				−0.000007390277	−0.004791009708
a_{10}					−0.000013063429

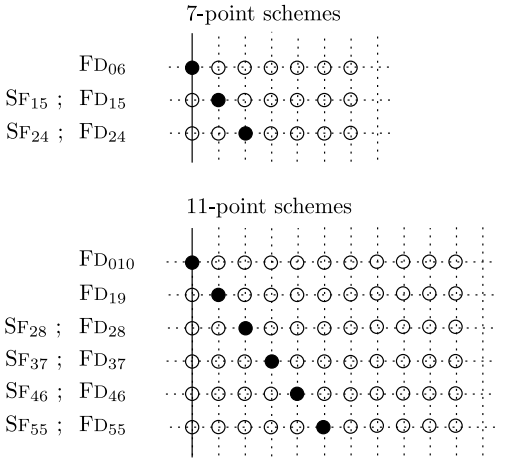

Fig. 12. Stencils and names of the non-centered finite differences F_{DPQ} and selective filters S_{FPQ}.

The schemes F_{D28}, F_{D19} and F_{D010} are more asymmetric are thus more dispersive: their dispersion limits are about five points per wavelength. As for the dissipation limits, they are about five points per wavelength for the schemes F_{D46}, F_{D37}, F_{D28} and F_{D19}, ranging from $\lambda/\Delta x = 4.30$ for the F_{D37} scheme up to $\lambda/\Delta x = 6.87$ for the F_{D19} scheme. Dispersion limit of the off-centered finite differences F_{D010} is about 10 points per wavelength. This scheme is nevertheless used at only one mesh point and the overall accuracy of the eleven-point non-centered schemes is thus set to five points per wavelength.

The present limits of accuracy in dispersion and dissipation demonstrate that non-centered eleven-point finite differences resolve accurately waves with at least five points per wavelength. Smaller wavelengths, which might lead to instabilities when they are amplified, must be removed by selective filtering.

3.2. Selective filters

Non-centered selective filtering of a function f can be processed on a uniform grid (x_i) so that

$$f^d(x_i) = f(x_i) - \sigma \sum_{j=-P}^{Q} d_j f(x_i + j\Delta x), \tag{24}$$

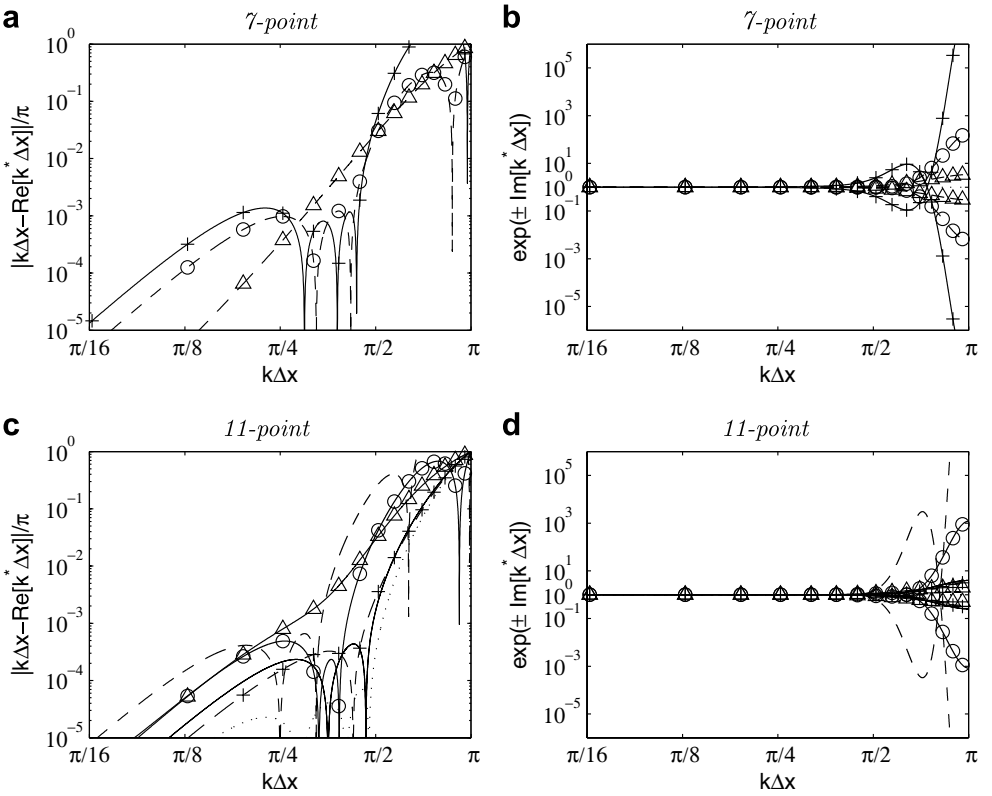

Fig. 13. Boundary finite differences. (a) Dispersion, and (b) dissipation of the seven-point schemes: — △ — FD_{24}, — ⊖ — FD_{15}, —+— FD_{06}; (c) dispersion, and (d) dissipation of the eleven-point schemes, as functions of the wave number $k\Delta x$: ··· FD_{55}, — FD_{46}, — + — FD_{37}, —△— FD_{28}, —⊖— FD_{19}, – – – FD_{010}.

Table 11
Dispersion and dissipation limits of the eleven-point non-centered finite differences, in points per wavelength $\lambda/\Delta x = 2\pi/k\Delta x$

	Dispersion $\lvert k\Delta x - \mathscr{R}e(k^*\Delta x)\rvert/\pi < 5\times 10^{-3}$	Dissipation $\lvert 1 - \mathrm{e}^{\mathscr{I}m(k^*\Delta x)}\rvert < 5\times 10^{-3}$
	$\lambda/\Delta x$	$\lambda/\Delta x$
FD_{55}	3.51	0
FD_{46}	3.77	4.46
FD_{37}	3.82	4.30
FD_{28}	5.15	6.04
FD_{19}	4.60	6.87
FD_{010}	5.59	10.12

where f^d is the filtered function, Δx is the mesh spacing, d_j are the coefficients of the filter, and σ is a constant taken between 0 and 1 defining the filtering strength. To design the filter and to investigate its properties, σ is chosen to be equal to 1, its maximum value. Consider the Fourier transform in space of (24) to compute the transfer function of the filtering:

$$G(k\Delta x) = 1 - \sum_{j=-P}^{Q} d_j \mathrm{e}^{\mathrm{i}jk\Delta x}. \tag{25}$$

The filter is made of second order by imposing $G(\pi) = 0$, and $G(k) = 1 + \mathcal{O}(k\Delta x^2)$ with a Taylor expansion as $k\Delta x \to 0$. Standard explicit non-centered filters, designed by maximizing the formal order as $k\Delta x \to 0$, are unstable [16]. Therefore, in the present work, the coefficients d_j of the filters are determined so that

$$|G(k\Delta x)| < 1, \quad \text{for } k\Delta x > 0 \tag{26}$$

in order to ensure stability. The coefficients d_j are optimized in the spectral space by minimizing the following integral error:

$$\int_{\pi/16}^{\pi/2} [(1-\alpha)|1 - G(k\Delta x)| + \alpha|\phi_G(k\Delta x)|] \frac{\mathrm{d}(k\Delta x)}{k\Delta x} \tag{27}$$

where ϕ_G is the argument of the frequency response function and the constant α is taken between 0 and 1 depending on the filters. This parameter α, whose values are given in Table 8, is chosen to balance the emphasis put on dispersion and on dissipation during the optimization process. The optimization procedure shows a sensitivity to α similar to that observed during the optimization of the finite differences in Section 3.1. The integral error is calculated on the interval corresponding to the wave numbers to be optimized: $\pi/16 \leqslant k\Delta x \leqslant \pi/2$. In this work, second-order seven- and eleven-point optimized non-centered selective filters have been designed. Their coefficients are given in Tables 12 and 13 and the filter names are defined in the same way as finite difference names, i.e. SF_{PQ} as shown in Fig. 12. The present optimization failed in providing completely off-centered filters involving seven and eleven points. However, a four-point stencil filter will be proposed at the end of the present subsection. Moreover, the optimization yields an eleven-point filter SF_{19} introducing excessive dissipation over a large range of wavelengths. A seven-point filter SF_{15} will be therefore used instead of SF_{19}.

The amount of dissipation $1 - |G(k\Delta x)|$ and the phase error $|\phi_G(k\Delta x)|$ of the seven-point and the eleven-point filters are presented in Figs. 14a and b, and in Figs. 14c and d, in logarithmic scales as functions of $k\Delta x$. For comparison, the features of the eleven-point centered optimized filter of Bogey and Bailly [4] are also plotted in Fig. 14c. As shown in Figs. 14a and c, the low wave numbers are not significantly damped. The amount of dissipation is indeed lower than 5×10^{-3} up to about $k\Delta x = \pi/2.5$, i.e. for five points per wavelength, for all

Table 12
Coefficients of the seven-point non-centered selective filters

	SF_{24}	SF_{15}
d_{-2}	0.032649010764	
d_{-1}	−0.143339502575	−0.085777408970
d_0	0.273321177980	0.277628171524
d_1	−0.294622121167	−0.356848072173
d_2	0.186711738069	0.223119093072
d_3	−0.062038376258	−0.057347064865
d_4	0.007318073189	−0.000747264596
d_5		−0.000027453993

Table 13
Coefficients of the eleven-point non-centered selective filters

i	SF_{46}	SF_{37}	SF_{28}
d_{-4}	0.008391235145		
d_{-3}	−0.047402506444	−0.000054596010	
d_{-2}	0.121438547725	0.042124772446	0.052523901012
d_{-1}	−0.200063042812	−0.173103107841	−0.206299133811
d_0	0.240069047836	0.299615871352	0.353527998250
d_1	−0.207269200140	−0.276543612935	−0.348142394842
d_2	0.122263107844	0.131223506571	0.181481803619
d_3	−0.047121062819	−0.023424966418	0.009440804370
d_4	0.009014891495	0.013937561779	−0.077675100452
d_5	0.001855812216	−0.024565095706	0.044887364863
d_6	−0.001176830044	0.013098287852	−0.009971961849
d_7		−0.002308621090	0.000113359420
d_8			0.000113359420

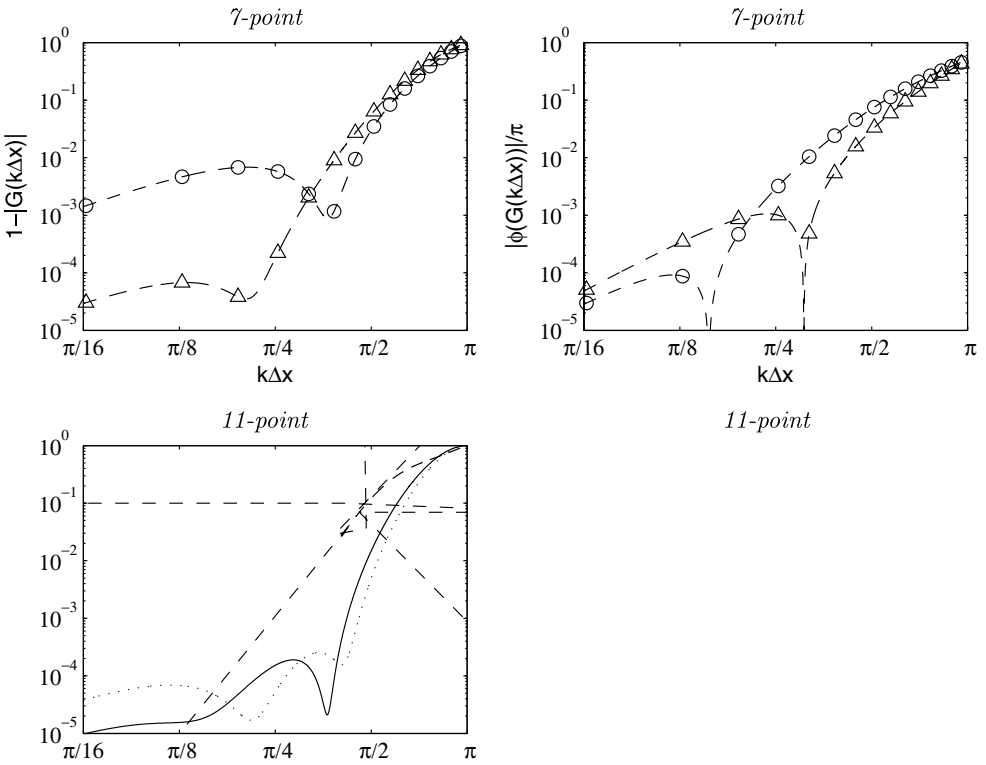

the non-centered filters except for the seven-point filter $S_{F_{15}}$ which is slightly more dissipative. The amount of dissipation provided by this filter $S_{F_{15}}$ remains however close to 5×10^{-3} for wave numbers such that $\pi/16 \leqslant k\Delta x \leqslant \pi/2.5$. For all the filters, the amount of dissipation is important for waves with $k\Delta x \sim \pi$, in order to remove grid-to-grid oscillations. The phase errors, plotted in Figs. 14b and d for the different filters, are shown to be lower than 5×10^{-3} up to about $k\Delta x < \pi/2.5$, i.e. down to five points per wavelength. For higher wave numbers, $k\Delta x \sim \pi$, the phase errors become significant but these high-frequency waves are damped.

The filter properties are reported in Table 14. Limits of accuracy in amplitude and in phase are estimated using the criteria $1 - |G(k\Delta x)| < 5\times10^{-3}$ and $|\phi_G(k\Delta x)|/\pi < 5\times10^{-3}$. The dissipation limits of the filters $S_{F_{46}}$, $S_{F_{37}}$ and $S_{F_{28}}$ range from four to six points per wavelength. The filter $S_{F_{15}}$ is more dissipative with a limit of 14 points per wavelength, but it is used only at one mesh point and its amount of dissipation is close to 5×10^{-3}

for $k\Delta x \leqslant \pi/3$ as shown in Fig. 14a. The accuracy limit in phase of the filter S_{F46}, whose stencil is very weakly asymmetric, is close to two points per wavelength. For the filter S_{F37}, the limit of accuracy in phase is about five points per wavelength, while it is close to seven points per wavelength for the schemes S_{F28} and S_{F15}. The overall accuracy limit may nevertheless be set to five points per wavelength as the non-centered schemes are implemented on a small number of mesh points.

From a practical point of view, completely off-centered selective filters are needed to avoid numerical instabilities for realistic flow configurations. The optimization process described above provided off-centered seven- and eleven-point filters displaying excessive damping. A second-order four-point filter, denoted by S_{F03}, has nevertheless been designed by putting emphasis only on the amplitude accuracy during optimization. Its coefficients are provided in Table 15. The filter properties in the Fourier space are presented in Fig. 15. As shown by the dispersion error in Fig. 15b, the filter is less accurate in phase with respect to the other boundary filters. The amplitude accuracy is similar to the accuracy of the other non-centered filters. The amount of dissipation, plotted in Fig. 15a, is indeed lower than 5×10^{-3} up to wave numbers about $k\Delta x = \pi/2.5$. The accuracy limit in amplitude based on the criterion $1 - |G(k\Delta x)| < 5\times10^{-3}$ yields for instance $\lambda/\Delta x = 5.41$, corresponding to waves with about five points per wavelength. For small wave numbers, the amount of dissipation of the wall filter is however one order of magnitude larger with respect to the other boundary filters. Therefore, in what follows, it will be applied with a filtering strength 10 times lower than the other filters.

3.3. One-dimensional propagation problem

A linear acoustic problem is considered by the solving the dimensionless equation:

$$\begin{aligned} &\frac{\partial u}{\partial t} + \frac{\partial p}{\partial x} = 0, \\ &\frac{\partial p}{\partial t} + \frac{\partial u}{\partial x} = 0 \end{aligned} \tag{28}$$

Table 15
Coefficients of the four-point completely off-centered selective filter S_{F03}

i	S_{F03}
d_0	0.320882352941
d_{-1}	−0.465
d_{-2}	0.179117647059
d_{-3}	−0.035

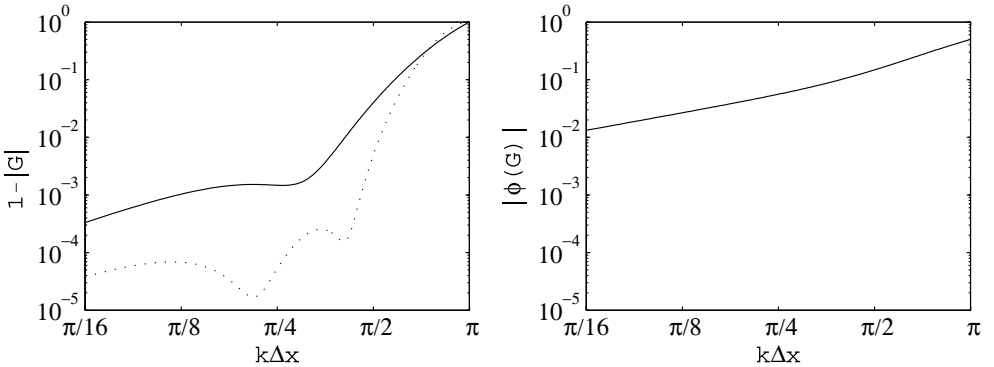

Fig. 15. Boundary selective filter S_{F03}. (a) Amount of dissipation, and (b) phase of the filter, as a function of the wave number $k\Delta x$: ⋯ S_{F55}, — S_{F03}.

on a domain extending from $x = -50$ to $x = 50$ and discretized by a uniform grid with $\Delta x = 1$. Wall boundary conditions are enforced at the boundaries of the computation domain, i.e.

$$\frac{\partial p}{\partial x} = 0 \quad \text{at } x = \pm 50. \tag{29}$$

Numerically, $\partial p/\partial x$ is set to zero at the boundaries and $\partial u/\partial x$ is computed using the interior points. The following initial disturbance is defined at $t = 0$:

$$\begin{cases} u = 0, \\ p = \cos\left(\frac{2\pi x}{a\Delta x}\right) \exp\left[-\ln(2)\left(\frac{x}{b\Delta x}\right)^2\right] \end{cases} \tag{30}$$

with $a = 8$ and $b = 12$. It is plotted in Fig. 16a, and Fig. 16b shows the normalized power spectral density of the initial perturbation. The initial perturbation is a wave with a dominant component discretized by eight points per wavelength.

The system of equations (28) is solved up to time $t = 200$. At this time position, each part of the initial disturbance, the left-running and the right-running part, merges after two reflections into a wave identical to the initial perturbation. Time integration is performed using an optimized six-stage Runge–Kutta algorithm [4], and the eleven-point optimized finite differences and selective filtering of Bogey and Bailly [4] are used for centered spatial derivatives. The CFL number is set to 0.8, i.e. $\Delta t = 0.8$. Two filtering strengths, $\sigma = 0.2$ and $\sigma = 0.8$, are used. The problem is first solved with centered schemes at the boundaries. The centered finite differences and selective filters are the standard schemes whose coefficients are computed by maximizing the order of accuracy. At the last point of the computational domain, centered schemes can no longer be used and a two-point off-centered stencil is implemented here. A sketch of the schemes is provided in Fig. 17. The boundary schemes and filters are then progressively introduced to illustrate their respective accuracy.

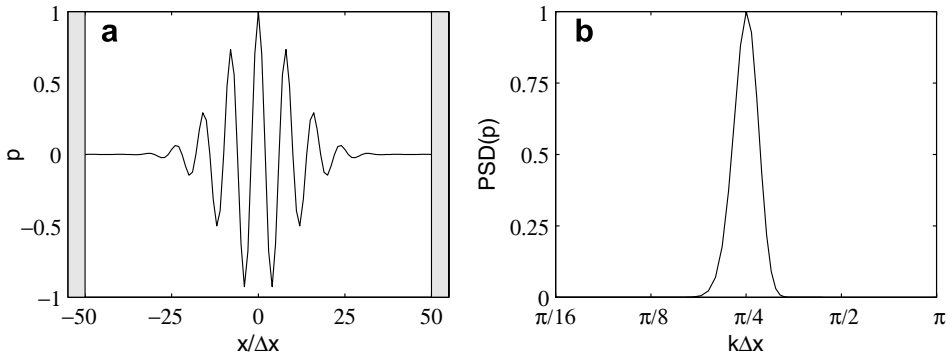

Fig. 16. (a) Initial pressure perturbation and (b) normalized power spectral density of the initial perturbation. The gray stripes represent the wall boundaries.

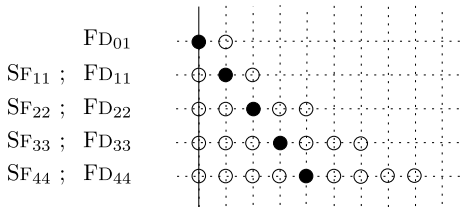

Fig. 17. Stencils and names of the centered finite differences and filters and of the off-centered finite differences $F_{D_{01}}$.

One should notice that in these calculations, no completely off-centered filtering is used at the first and last point of the computational domain. Finally, the error is computed with the L_2-norm as

$$L_2 = \sqrt{\frac{\sum (p - p_e)^2}{\sum p_e^2}}, \tag{31}$$

where p and p_e are, respectively, the computed and the exact vector solution. Note that better results are expected using the non-centered optimized large-stencil schemes than the centered schemes reduced to second-order near the boundaries. Stable explicit decentered filters are however not available in the literature for large stencils, and a direct comparison with an alternative similar method is therefore difficult. A robust formulation involving an explicit filtering is however required for practical applications where Navier–Stokes equations with wall boundary conditions are solved. It will be shown by this test case and the one shown in the next section, that the present boundary schemes and filters are capable of preserving acoustics during such simulations.

Computed solutions are plotted in Fig. 18. Figs. 18(1)a and (1)b show the solutions obtained using only centered finite differences and filters. The waves are seen to be here strongly damped, both for the filtering strengths $\sigma = 0.2$ and $\sigma = 0.8$. In Figs. 18(2)a and (2)b, the centered schemes F_{D01}, F_{D11} and S_{F11} are replaced by the non-centered schemes F_{D010}, F_{D19} and S_{F15}. The computed solutions are then in good agreement with the exact solution. We can however notice that, unlike the solution computed with $\sigma = 0.2$ in Fig. 18(2)a, the solution computed with $\sigma = 0.8$ in Fig. 18(2)b is slightly damped. Finally the solutions obtained using only the non-centered schemes and filters at the boundaries are presented in Figs. 18(3)a and (3)b. In this case, increasing filtering strength from $\sigma = 0.2$ (Fig. 18(3)a) to $\sigma = 0.8$ (Fig. 18(3)b) does not significantly affect the solution amplitude. The filtering strength is thus shown to have very little influence on the resolved wave numbers.

The error is reported in Table 16 for various configurations of finite differences and selective filters. From left to right columns, the centered schemes and filters are progressively replaced by the non-centered schemes. The use of only centered schemes except F_{D01} or F_{D010} at the final point generates a significant error which rises as the filtering strength is increased, as shown in the two leftmost columns. Moreover, substituting finite differences F_{D01} by finite differences F_{D010} appears not to produce a notable improvement of accuracy, which suggests that the main part of errors is due to the centered schemes. When the schemes F_{D19} and S_{F15} are introduced, instead of F_{D11} and S_{F11}, the gain in accuracy is important. In this case, the errors are found to decrease by about one order of magnitude for $\sigma = 0.2$ and for $\sigma = 0.8$ (third column from the left). When the non-centered schemes F_{D28} and S_{F28} are then also implemented, the errors are similar to those of the former configuration (fourth column from the left). When the schemes F_{D37} and S_{F37} are introduced instead of F_{D33} and S_{F33}, the error is divided roughly by three for $\sigma = 0.2$ and by two for $\sigma = 0.8$ (fifth column from the left). There is no further appreciable change when the schemes F_{D46} and S_{F46} are also implemented (rightmost column). Finally, in the present test case, using the non-centered schemes instead of the centered schemes at the boundaries improves the accuracy by one order of magnitude both for $\sigma = 0.2$ and for $\sigma = 0.8$.

The test case is now solved using the off-centered filter S_{F03} at the first and last point of the computational domain. The other boundary points are treated using the eleven-point boundary filters and finite difference schemes as in Figs. 18(3)a and 18(3)b. In practical configurations, the filter S_{F03} is implemented for stability purposes only. According to Fig. 15a, for $k\Delta x < \pi/2.5$, the amount of dissipation of the off-centered filter is one order of magnitude larger compared to the dissipation of the eleven-point centered filter S_{F55}. Thus, to avoid extra-damping of the perturbations, the filtering strength used for the filter S_{F03}, referred to as σ_w, is chosen to be 10 times lower than the filtering strength σ used at the other mesh points. Two computations are performed here: one using $\sigma = 0.2$, and the other with $\sigma = 0.8$, yielding respectively $\sigma_w = 0.02$ and $\sigma_w = 0.08$ for the wall filtering. The results are plotted in Fig. 19a for $\sigma = 0.2$, and in Fig. 19b for $\sigma = 0.8$. For $\sigma = 0.2$, the calculated perturbation fits very well the exact solution. The solution provided for $\sigma = 0.8$ in Fig. 19b is still in good agreement with the exact solution. The dissipation is low and the accuracy is of the same order to that of the solution in Fig. 18(3)b, which is obtained for $\sigma = 0.8$ using the boundary schemes and without the off-centered filter.

3.4. Scattering of sound waves by a cylinder

A two-dimensional test case, extracted from the Second Computational Aeroacoustics Workshop [22], is finally used to give a practical illustration of the influence of the numerical schemes used near solid boundaries on the overall quality of simulation results. In this test case, a periodic acoustic source is scattered by a circular cylinder of diameter $D = 1$ placed at the origin. The source is given by

$$S(x,y,t) = \exp\left[-\ln 2\,\frac{(x-x_c)^2 + (y-y_c)^2}{b^2}\right]\sin(\omega t) \tag{32}$$

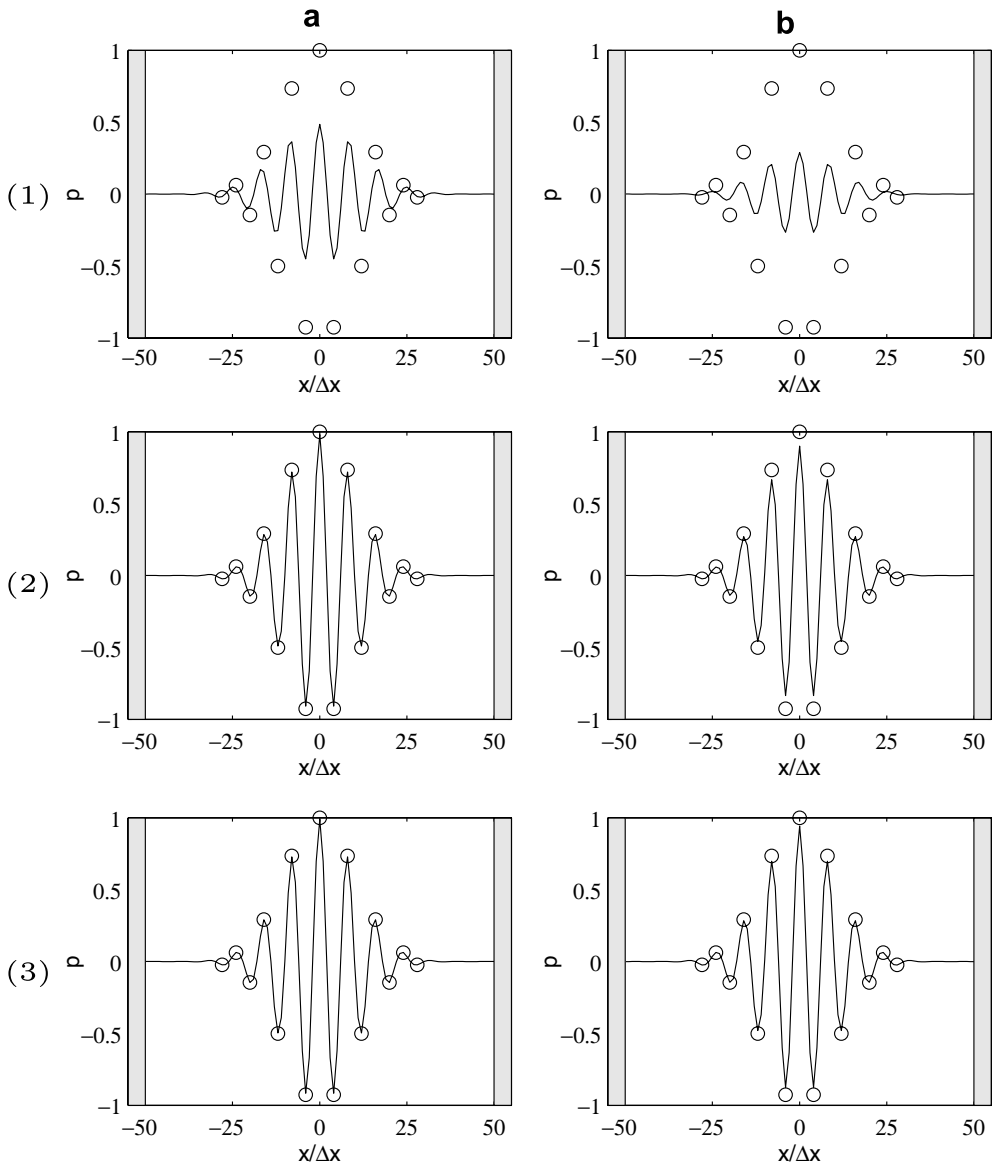

Fig. 18. Computed pressure for the reflection test case. The gray stripes represent the wall boundaries. (a) $\sigma = 0.2$. (b) $\sigma = 0.8$. (1) centered finite differences and centered selective filters. (2) the centered schemes F_{D01}, F_{D11} and S_{F11} are replaced by F_{D010}, F_{D19} and S_{F15}. (3) boundary schemes. —, computed solution; ○, exact solution.

Table 16
Reflection test problem

	F_{D44} and S_{F44} F_{D33} and S_{F33} F_{D22} and S_{F22} F_{D11} and S_{F11} F_{D01}	F_{D44} and S_{F44} F_{D33} and S_{F33} F_{D22} and S_{F22} F_{D11} and S_{F11} $\mathbf{F_{D010}}$	F_{D44} and S_{F44} F_{D33} and S_{F33} F_{D22} and $\mathbf{S_{F22}}$ $\mathbf{F_{D19}}$ and $\mathbf{S_{F15}}$ $\mathbf{F_{D010}}$	F_{D44} and S_{F44} F_{D33} and S_{F33} $\mathbf{F_{D28}}$ and $\mathbf{S_{F28}}$ $\mathbf{F_{D19}}$ and $\mathbf{S_{F15}}$ $\mathbf{F_{D010}}$	F_{D44} ans S_{F44} $\mathbf{F_{D37}}$ and $\mathbf{S_{F37}}$ $\mathbf{F_{D28}}$ and $\mathbf{S_{F28}}$ $\mathbf{F_{D19}}$ and $\mathbf{S_{F15}}$ $\mathbf{F_{D010}}$	$\mathbf{F_{D46}}$ and $\mathbf{S_{F46}}$ $\mathbf{F_{D37}}$ and $\mathbf{S_{F37}}$ $\mathbf{F_{D28}}$ and $\mathbf{S_{F28}}$ $\mathbf{F_{D19}}$ and $\mathbf{S_{F15}}$ $\mathbf{F_{D010}}$
$\sigma = 0.2$	0.53	0.35	0.02	0.03	0.01	0.01
$\sigma = 0.8$	0.72	0.85	0.10	0.10	0.06	0.05

L_2 error for various finite-difference and selective-filter configurations at the domain boundaries. Leftmost column: use of the centered schemes except F_{D01} at the wall point; rightmost column: use of the non-centered schemes at the boundary points; from left to right: non-centered schemes are progressively used instead of the centered schemes. The optimized non-centered schemes are represented in bold.

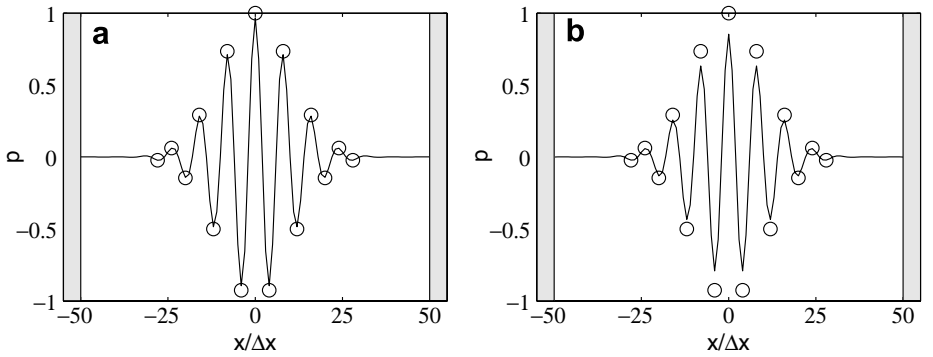

Fig. 19. Computed pressure for the reflection test case solved with the boundary schemes and the filter S_{F03}. The gray stripes represent the wall boundaries. (a) $\sigma = 0.2$, (b) $\sigma = 0.8$. The filtering strength at the wall in both cases is $\sigma/10$. —, computed solution; ○, exact solution.

with $x_c = 4D$, $y_c = 0$, $\omega = 8\pi$, and the Gaussian half-width of the source $b = 0.2$. A complex diffraction pattern is generated by this setup, and both high computational accuracy and high stability are necessary to match the analytical directivity pattern of the scattered acoustic field. As an illustration, Fig. 20a shows an instantaneous view of the sound field around the cylinder. It should be noted that although the original test case was published for the linearized Euler equations, the full nonlinear Euler equations in curvilinear coordinates are resolved in this work, as detailed in [17].

The test case is resolved with two different boundary implementations, on identical cylindrical grids. In all simulations, the free field zone is solved with the explicit centered eleven-point finite differences and filters of Bogey and Bailly [4], and the radial spacing is fixed to eight points per wavelength. A six-stage low-storage optimized Runge–Kutta scheme [4] is used for time integration. The computational grid is composed of 280 points in the radial direction and 720 points in the azimuthal direction. The large number of points in the latter direction is imposed by the geometry of the test case. Indeed, the 720 points give an azimuthal discretization of just over 7 points per wavelength at the source, because of the relatively large distance of $4D$ separating the source from the cylinder. In the first wall approach, the radial direction in the near-cylinder zone is resolved with centered finite differences and filters of progressively smaller stencil size, except for the wall points where two-point finite differences and filters are used. The second approach makes use of the non-centered optimized schemes proposed in Sections 3.1 and 3.2, including the off-centered filter S_{F03}.

The two different wall implementations are tested with two filtering strength configurations: $\sigma = 0.2$ and $\sigma = 0.8$. In both cases, the filtering strength at the wall points is set to $\sigma/10$. Figs. 21a and b show the directivities $D = r\overline{p'^2}$ as a function of the angle θ between 90° and 180°, at a distance of $r/D = 7.5$ from the origin, resulting from the computations performed with $\sigma = 0.2$. The directivity computed with the centered boundary treatment deviates noticeably from the analytical solution. The rms values obtained with the centered schemes, shown in Fig. 21a, are notably lower than those given by the analytical solution, indicating that

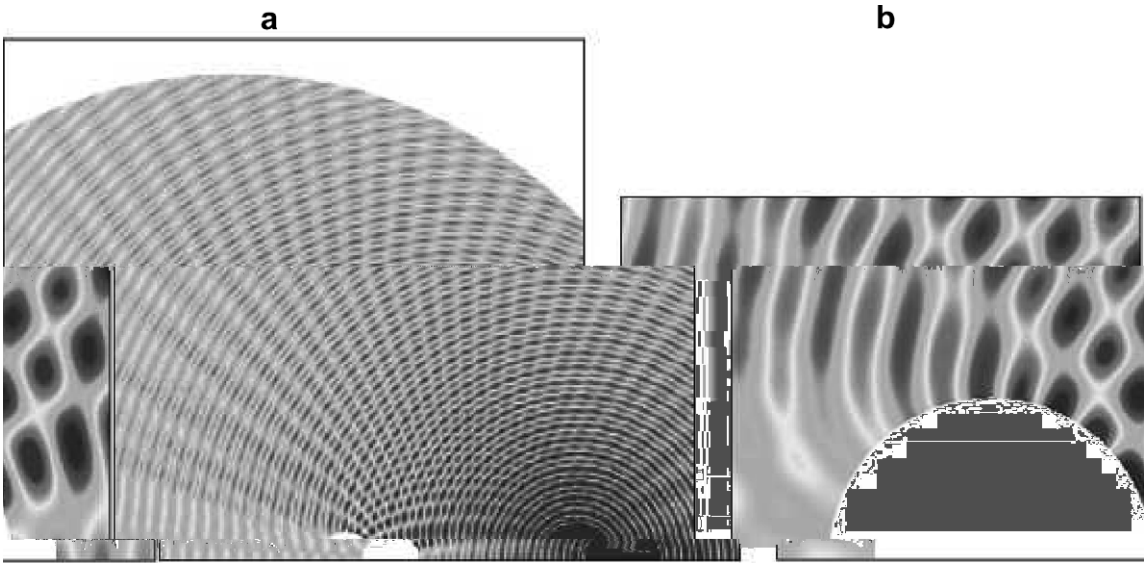

Fig. 20. Instantaneous views of the scattered pressure field: (a) full domain, (b) close-up view around the cylinder, obtained with the optimized non-centered wall schemes for a filtering strength of $\sigma = 0.2$. The filtering strength at the wall is $\sigma/10$.

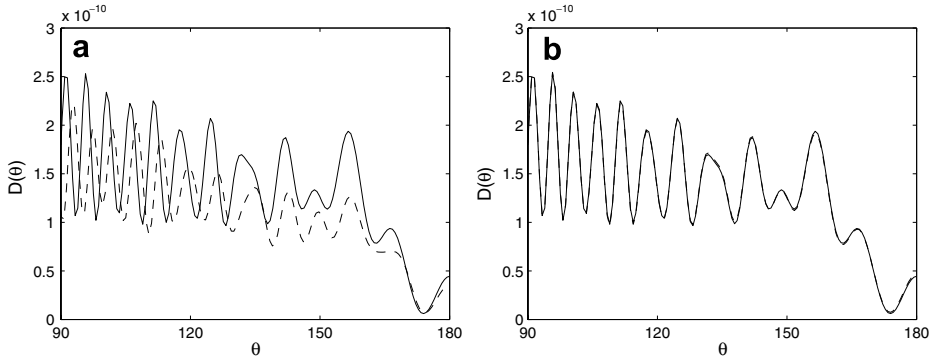

Fig. 21. Directivity $D(\theta) = r\overline{p'^2}$ at $r/D = 7.5$. (a) — analytical solution, – – – solution computed with centered schemes and with a filtering strength of $\sigma = 0.2$. (b) — analytical solution, – – – solution computed with optimized non-centered schemes and with a filtering strength of $\sigma = 0.2$. The filtering strength at the wall is $\sigma/10$.

the additional dissipation introduced by the wall treatment has a strong impact on the far-field pressure level. Moreover, the oscillations in the directivity are much less pronounced. This can be explained by noting that the undesirable dissipation induced by the centered filters affects only the scattered field and not the direct acoustic field, thus reducing the effects of interference between the two fields on the directivity. Finally, the locations of the directivity peaks are strongly shifted, due to the high dispersion introduced by the low-order centered finite differences. The optimized non-centered schemes, on the other hand, give results that match the analytical solution very well in Fig. 21b. Indeed, the relative error on the computed directivity remains under 1%. A close-up view of the pressure field around the cylinder, generated with the non-centered optimized schemes, can also be seen in Fig. 20b, showing the absence of spurious oscillations which are often generated by high-order solid boundary conditions.

The results of the two simulations with the stronger filtering value of $\sigma = 0.8$, shown in Figs. 22a and b, demonstrate the advantages of the optimized schemes proposed in this work over the standard centered approach. The results obtained with the optimized schemes, presented in Fig. 22b, are indeed almost identical

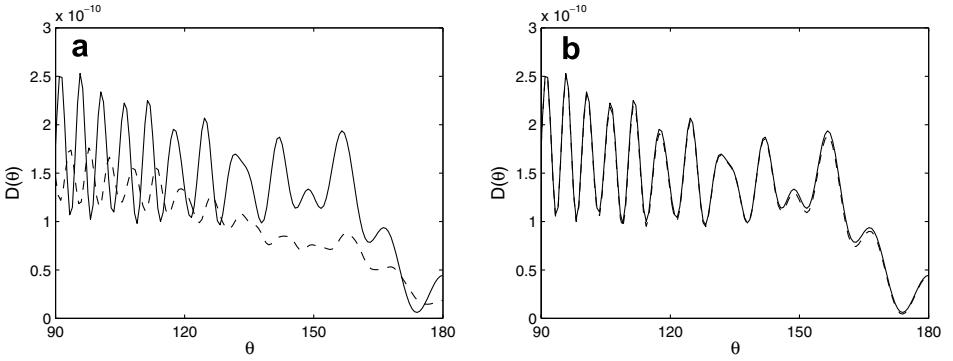

Fig. 22. Directivity $D(\theta) = r\overline{p'^2}$ at $r/D = 7.5$. (a) — analytical solution, – – – solution computed with centered schemes and with a filtering strength of $\sigma = 0.8$. (b) — analytical solution, – – – solution computed with optimized non-centered schemes and with a filtering strength of $\sigma = 0.8$. The filtering strength at the wall is $\sigma/10$.

to those obtained with the smaller filtering strength. The very slightly lower rms values obtained with $\sigma = 0.8$ can at least partly be attributed to the dissipation inherent – albeit very low – to the centered eleven-point filter used in the free-field region. Indeed, the time spent by each wavefront in the near-cylinder region is very small compared to its free-field propagation time. The results obtained with the centered approach suffer much more from the increase in the filtering strength, as is illustrated by Fig. 22a. The rms directivity is strongly attenuated, and the oscillations in the directivity are further reduced. The centered filters are not sufficiently selective, and thus they dissipate the physical waves as well as the spurious numerical oscillations generated by the wall boundary condition.

This test case provides a good illustration of the role played by the numerical schemes used to resolve a solid boundary condition. Standard centered finite differences are shown here to lead to unsatisfactory results, and the unduly high dissipation on long wavelengths imposed by the standard centered filters is also shown to have a considerable impact on the quality of the computational results. The non-centered optimized finite differences and filters proposed in this work exhibit neither of these undesirable aspects, and give results in excellent agreement with the analytical solution.

4. Conclusion

Explicit schemes have been proposed for local features of the computational domain. High-order finite differences and selective filters permitting waves to travel from uniform Δx-mesh to uniform $2\Delta x$-mesh have first been designed. The analysis of dispersion and dissipation properties and the evaluation of accuracy limits demonstrated that these schemes resolve accurately waves with at least five points per wavelength. They can be useful for instance to compute the far-field propagation of sound waves generated by turbulent flows. Non-centered finite differences and selective filters for boundary conditions have also been designed by minimizing their dispersion and dissipation errors. These schemes are highly accurate for waves with at least five points per wavelength. For reflection test problems, they provided results showing the spectacular improvement of precision with respect to the centered schemes. A test case involving acoustic scattering around a cylinder demonstrated in particular the ability of these boundary schemes to yield an accurate solution for a complex configuration.

References

[1] C.K.W. Tam, Computational aeroacoustics: issues and methods, AIAA J. 33 (10) (1995) 1788–1796.
[2] C.K.W. Tam, J.C. Webb, Dispersion-relation-preserving finite difference schemes for computational acoustics, J. Comput. Phys. 107 (1993) 262–281.
[3] S.K. Lele, Compact finite difference schemes with spectral-like resolution, J. Comput. Phys. 103 (1992) 16–42.
[4] C. Bogey, C. Bailly, A family of low dispersive and low dissipative explicit schemes for flow noise and noise computations, J. Comput. Phys. 194 (2003) 194–214.

[5] C. Bogey, C. Bailly, D. Juvé, Noise investigation of a high subsonic, moderate Reynolds number jet using a compressible LES, Theor. Comput. Fluid Dyn. 16 (4) (2003) 273–297.
[6] C. Bogey, C. Bailly, Computation of a high Reynolds number jet and its radiated noise using large eddy simulation based on explicit filtering, Comput. Fluids 35 (10) (2006) 1344–1358.
[7] C.K.W. Tam, K.A. Kurbatskii, Multi-size-mesh multi-time-step dispersion-relation-preserving scheme for multiple-scales aero-acoustics problems, Int. J. Comput. Fluid Dyn. 17 (2) (2003) 119–132.
[8] M.R. Visbal, D.V. Gaitonde, Higher-order-accurate methods for complex unsteady subsonic flows, AIAA J. 37 (10) (1999) 1231–1239.
[9] D.V. Gaitonde, M.R. Visbal, Padé-type higher-order boundary filters for the Navier–Stokes equations, AIAA J. 38 (11) (2000) 2103–2112.
[10] M.R. Visbal, P.E. Morgan, D.P. Rizetta, A time-implicit high-order compact differencing and filtering scheme for large-eddy simulation, Int. J. Numer. Meth. Fluids 42 (2003) 665–693.
[11] D.V. Gaitonde, M.R. Visbal, Advances in the application of high-order techniques in simulation of multi-disciplinary phenomena, Int. J. Comput. Fluid Dyn. 17 (2) (2003) 95–106.
[12] C.K.W. Tam, Z. Dong, Wall boundary conditions for high-order finite-difference schemes in computational aeroacoustics, Theor. Comput. Fluid Dyn. 6 (1994) 303–322.
[13] H. Shen, C.K.W. Tam, Three-dimensional numerical simulation of the jet screech phenomenon, AIAA J. 40 (1) (2002) 33–41.
[14] D.P. Lockard, K.S. Brentner, H.L. Atkins, High-accuracy algorithms for computational aeroacoustics, AIAA J. 33 (2) (1995) 246–251.
[15] M. Zhuang, R.F. Chen, Optimized upwind dispersion-relation-preserving finite difference scheme for computational aeroacoustics, AIAA J. 36 (11) (1998) 2146–2148.
[16] M.R. Visbal, D.V. Gaitonde, Very high-order spatially implicit schemes for computational acoustics on curvilinear meshes, J. Comput. Acoust. 9 (4) (2001) 1259–1286.
[17] O. Marsden, C. Bogey, C. Bailly, High-order curvilinear simulations of flows around non-Cartesian bodies, J. Comput. Acoust. 13 (4) (2005) 731–748.
[18] O. Marsden, C. Bogey, C. Bailly, Noise radiated by a high-Reynolds-number 3-D airfoil, in: 11th AIAA/CEAS Aeroacoustics Conference, Monterey, CA, USA, 23–25 May, AIAA Paper 2005-2817.
[19] J. Lighthill, Waves in Fluids, Cambridge University Press, Cambridge, 1978.
[20] L.N. Trefethen, Group velocity in finite difference schemes, SIAM Rev. 24 (2) (1982) 113–136.
[21] C.A.J. Fletcher, Computational Techniques for Fluid Dynamics, Springer, Berlin, 1998.
[22] Proceedings of the second Computational AeroAcoustics (CAA) Workshop on Benchmark Problems, NASA Langley Research Center, Hampton, Virginia CP 23681-0001, 1997.